An analytical method for selecting the optimal nozzle external geometry for fluid dynamic gauging

J.M. Peralta[1,2], Y.M.J. Chew[3], D.I. Wilson[2*]

[1]Instituto de Desarrollo Tecnológico para la Industria Química (INTEC), Universidad Nacional del Litoral – CONICET, Güemes 3450, S3000GLN, Santa Fe, Argentina.

[2]Department of Chemical Engineering and Biotechnology, University of Cambridge, New Museums Site, Pembroke Street, Cambridge, CB2 3RA, UK

[3]Department of Chemical Engineering, University of Bath, Building 9 West, Claverton Down, Bath, BA2 7AY, UK

Abstract

Fluid dynamic gauging (FDG) was developed to measure, in situ and in real time, the thickness of a soft deposit layer immersed in a liquid without contacting the surface of the layer. An analysis based on the lubrication assumption for the flow patterns in the space between the nozzle and the surface being gauged yielded analytical expressions for the relationships between the main flow variables and system parameters. Nozzle shapes for particular pressure, pressure gradient and shear stress profiles could then be identified. The effect of flow rate, nozzle geometry and nozzle position on the pressure beneath the nozzle and shear stress on the gauged surface showed very good agreement with computational fluid dynamics (CFD) simulations. Case studies presented include nozzle shapes for uniform pressure and shear stress profiles, which are useful for measuring the strength of soft deposit layers.

Keywords: CFD; Cleaning; Fluid Dynamic Gauging; Fluid mechanics; Fouling; Laminar flow.

* Corresponding author. Tel.: +44 1233 334791; fax:+44 1233 334796.
E-mail address: diw11@cam.ac.uk (D.I. Wilson).

1. Introduction

The deposition of films on process surfaces from a flowing liquid occurs in many industrial manufacturing processes. Some of these films are desired (*e.g.* chocolate coatings on biscuits) and some are unwanted (*e.g.* fouling layers in heat exchangers). In both cases, it is often important to measure the thickness and strength of these films. In the biotechnology and food sectors, these films are frequently soft and/or fragile and their state is strongly dependent on the presence of liquid, so that measurements of thickness and strength should be determined in situ and in real time particularly where the deposit is evolving. Portable, rapid, non-contact and precise techniques are needed.

Fluid dynamic gauging (FDG) is a relatively novel technique that was developed by Tuladhar *et al*. (2000) to estimate *in situ* and in real time the thickness of a soft deposit layer immersed in liquid without touching the surface of this layer. The concept consists of a nozzle that withdraws liquid from the region near the deposit surface, as shown in Figure 1. For a certain range of clearances between the nozzle and the surface (h), the flow rate ($\dot{m}$) through the nozzle is usefully sensitive to h (Figure 1(*b*)). The thickness of the deposit, δ, can be calculated from the difference in clearance between the nozzle and the deposit layer, h (inferred from the flow rate), and the position of the nozzle relative to the substrate, h_{init}, (established either by calibration or independent sensing). The technique provides high accuracy thickness measurement with a resolution of ± 5 μm with a sensing time of ≤ 5 s (Gordon *et al*., 2010).

Studies such as that by Chew *et al*., (2004a) have shown that FDG could also be used to quantify the strength of soft deposits. The gauge employs flows in the laminar regime,

allowing computational fluid dynamics (CFD) to be used to give reliable estimates of the flow field and stress distribution in the flow. Chew *et al*. quantified the strength of different tomato paste layers by measuring the deformation of the film following gauging at a known shear stress exerted by the gauge on the film. Thickness measurements were made at high clearance (low shear stress) and following exposure of the film to higher shear stresses induced by moving the nozzle closer to the film.

The stresses induced on the film by the gauging flow are determined by the liquid flow rate, clearance and also the external geometry of the nozzle. Peralta *et al*. (2011) demonstrated how the external shape of the nozzle could affect, very noticeably, the shear stress (τ_w) and pressure (p) profiles on a gauged surface. They identified geometries that produced interesting τ_w and p profiles such as linear, peaked or bimodal distributions. These types of profiles are attractive to FDG operation as they offer the opportunity to manipulate the forces exerted on a film by simply changing the nozzle. For example, an approximately constant erosion of the film can be produced under the nozzle rim when an even shear stress profile is used. Alternately, another shape could yield high sensitivity to clearance (measurement precision) while minimizing fluid shear.

Previous workers have employed computational fluid dynamics (CFD) simulations to estimate how the operating variables affect the important flow variables such as the profiles of shear stress and pressure exerted on the deposit (Chew *et al*., 2004b; Gu *et al*., 2009, 2011; Lister *et al*., 2011). The definition of the geometry and meshing is straightforward and simulations take a few minutes to converge on modern PCs (Peralta *et al*., 2011). Exploring nozzle geometries is time consuming, however, as the mesh must be re-defined for each simulation. This paper therefore explores the scope for analytically-based approaches to

77 investigate the impact of nozzle shape on FDG performance, to be used to identify likely
78 configurations for fine tuning by simulation.
79
80 A key feature of FDG operation (Figure 1(*b*)) is that the nozzle must be close to the film
81 surface in order to work properly, i.e. $h/d_t \leq 0.25$. The radial dimension under the nozzle
82 rim is much larger than the gap between the nozzle and the film which, when combined with
83 the laminar nature of the flow, suggests that analyses based on the lubrication
84 approximation should yield useful results. This approach was employed by Chew *et al*.
85 (2005) and later by Gu *et al*. (2009) to estimate the shear stress imposed on the surface. In
86 both cases shear stress distributions obtained from CFD simulations showed good
87 agreement with the analytical solution for a radial flow between two parallel disks obtained
88 by Middleman (1998) using lubrication theory. This paper extends the approach to consider
89 the effect of nozzle geometry.
90
91
92 **2. Theoretical approach**
93 **2.1. Equations of change**
94 The physical domain of interest is the gap between the nozzle and the gauged surface (Fig.
95 2). The equations of change, adapted to include the lubrication approximation, are written
96 in cylindrical co-ordinates following the procedure presented by Denn (1980). Only the
97 principal steps of the analysis are presented. The following assumptions are made: (*i*) steady
98 state; (*ii*) Newtonian fluid; (*iii*) the velocity component in the φ direction is negligibly
99 small; (*iv*) axisymmetry in φ; and (*v*) external forces are due to gravity and act only in the z
100 direction. These assumptions simplify the continuity (Eq. (1)) and Navier Stokes (Eqs. (2)
101 and (3)) equations to

$$\frac{1}{r}\frac{\partial}{\partial r}\left(rv_r\right)+\frac{\partial v_z}{\partial z}=0 \tag{1}$$

$$\rho\left(v_r\frac{\partial v_r}{\partial r}+v_z\frac{\partial v_r}{\partial z}\right)=-\frac{\partial p}{\partial r}+\mu\left[\frac{\partial}{\partial r}\left(\frac{1}{r}\frac{\partial}{\partial r}\left(rv_r\right)\right)+\frac{\partial^2 v_r}{\partial z^2}\right] \tag{2}$$

$$\rho\left(v_r\frac{\partial v_z}{\partial r}+v_z\frac{\partial v_z}{\partial z}\right)=-\frac{\partial p}{\partial z}+\mu\left[\frac{1}{r}\frac{\partial}{\partial r}\left(r\frac{\partial v_z}{\partial r}\right)+\frac{\partial^2 v_z}{\partial z^2}\right]+\rho g_z \tag{3}$$

Equations (1- 3) can be made non-dimensional using the following identities:

$$\tilde{r}=\frac{r}{r_o-r_i} \tag{4}$$

$$\tilde{z}=\frac{z}{h_o} \tag{5}$$

$$\tilde{v}_r=\frac{v_r}{U_o} \tag{6}$$

$$\tilde{v}_z=\frac{v_z}{V} \tag{7}$$

$$\tilde{p}=\frac{p-\rho g_z z}{\Pi} \tag{8}$$

where r_i and r_o are the internal and external radius of the nozzle, respectively; h_o is the clearance between the nozzle and the gauged surface at r_o, U_o is the mean velocity at the external radius calculated from the flow rate, and V and Π are the characteristic values for *z*-velocity and pressure that will be defined later. The use of these dimensionless variables

assists the order of magnitude analysis discussed below and allows the results to be condensed into general equations and a small number of figures.

Introducing Equations (4-8) into Equations (1-3) yields

$$\frac{1}{\tilde{r}}\frac{\partial}{\partial\tilde{r}}\left(\tilde{r}\tilde{v}_r\right)+\frac{V\left(r_o-r_i\right)}{U_o h_o}\frac{\partial\tilde{v}_z}{\partial\tilde{z}}=0 \tag{9}$$

$$\frac{\rho U_o^2}{\left(r_o-r_i\right)}\left[\tilde{v}_r\frac{\partial\tilde{v}_r}{\partial\tilde{r}}+\frac{V\left(r_o-r_i\right)}{U_o h_o}\tilde{v}_z\frac{\partial\tilde{v}_r}{\partial\tilde{z}}\right]=-\frac{\Pi}{\left(r_o-r_i\right)}\frac{\partial\tilde{p}}{\partial\tilde{r}}+\frac{\mu U}{h_o^2}\left[\left(\frac{h_o}{\left(r_o-r_i\right)}\right)^2\frac{\partial}{\partial\tilde{r}}\left(\frac{1}{\tilde{r}}\frac{\partial}{\partial\tilde{r}}\left(\tilde{r}\tilde{v}_r\right)\right)+\frac{\partial^2\tilde{v}_r}{\partial\tilde{z}^2}\right] \tag{10}$$

$$\frac{\rho U_o V}{\left(r_o-r_i\right)}\left[\tilde{v}_r\frac{\partial\tilde{v}_z}{\partial\tilde{r}}+\frac{V\left(r_o-r_i\right)}{U_o h_o}\tilde{v}_z\frac{\partial\tilde{v}_z}{\partial\tilde{z}}\right]=-\frac{\Pi}{h_o}\frac{\partial\tilde{p}}{\partial\tilde{z}}+\frac{\mu V}{h_o^2}\left[\left(\frac{h_o}{\left(r_o-r_i\right)}\right)^2\frac{1}{\tilde{r}}\frac{\partial}{\partial\tilde{r}}\left(\tilde{r}\frac{\partial\tilde{v}_z}{\partial\tilde{r}}\right)+\frac{\partial^2\tilde{v}_z}{\partial\tilde{z}^2}\right] \tag{11}$$

Denn (1980) presented a dimensional analysis of Eq. (9) which showed that the magnitude of the factor multiplying the derivative in the second term is $O\left[V\left(r_o-r_i\right)/\left(U_o h_o\right)\right]\cong 1$. Denoting $\varepsilon=h_o/\left(r_o-r_i\right)$, this gives $O(V)=O(\varepsilon U_o)$. This relation, based on the continuity equation and a dimensional analysis of the problem, shows a natural way to define V. Therefore, the definition of V used here will be $V=\varepsilon U_o$. Eq. (7) can then be written as $\tilde{v}_z=v_z/(\varepsilon U_o)$. Eq. (10) becomes

$$\mathrm{Re}\cdot\varepsilon\left(\tilde{v}_r\frac{\partial\tilde{v}_r}{\partial\tilde{r}}+\tilde{v}_z\frac{\partial\tilde{v}_r}{\partial\tilde{z}}\right)=-\frac{\Pi h_o\varepsilon}{\mu U_o}\frac{\partial\tilde{p}}{\partial\tilde{r}}+\varepsilon^2\frac{\partial}{\partial\tilde{r}}\left[\frac{1}{\tilde{r}}\frac{\partial}{\partial\tilde{r}}\left(\tilde{r}\tilde{v}_r\right)\right]+\frac{\partial^2\tilde{v}_r}{\partial\tilde{z}^2} \tag{12}$$

where the Reynolds number is defined as $\mathrm{Re}=\rho U_o h_o/\mu$.

The operating mode of the gauge requires the nozzle to be very close to the gauged surface such that ε is small, *i.e.* $\varepsilon^2 << 1$. The flow is in the laminar regime (discussed in Section 2.3), so that $\mathrm{Re}\cdot\varepsilon << 1$, and Eq. (12) becomes:

$$0 \cong -\frac{\Pi h_o \varepsilon}{\mu U_o}\frac{\partial \tilde{p}}{\partial \tilde{r}} + \frac{\partial^2 \tilde{v}_r}{\partial \tilde{z}^2} \tag{13}$$

From the order of magnitude of the terms in Eq. (13) (Denn, 1980), the parameter Π can be defined as $\Pi = \mu U_o / (h_o \varepsilon)$. Rearranging Eq. (11) gives

$$\mathrm{Re}\cdot\varepsilon^3\left(\tilde{v}_r\frac{\partial \tilde{v}_z}{\partial \tilde{r}} + \tilde{v}_z\frac{\partial \tilde{v}_z}{\partial \tilde{z}}\right) = -\frac{\partial \tilde{p}}{\partial \tilde{z}} + \varepsilon^4\frac{1}{\tilde{r}}\frac{\partial}{\partial \tilde{r}}\left(\tilde{r}\frac{\partial \tilde{v}_z}{\partial \tilde{r}}\right) + \varepsilon^2\frac{\partial^2 \tilde{v}_z}{\partial \tilde{z}^2} \tag{14}$$

Incorporating the relationships $\mathrm{Re}\cdot\varepsilon^3 << 1$, $\varepsilon^2 << 1$ and $\varepsilon^4 << 1$, gives the equations of change as

$$\frac{1}{\tilde{r}}\frac{\partial}{\partial \tilde{r}}\left(\tilde{r}\tilde{v}_r\right) + \frac{\partial \tilde{v}_z}{\partial \tilde{z}} = 0 \tag{15}$$

$$0 \cong -\frac{\partial \tilde{p}}{\partial \tilde{r}} + \frac{\partial^2 \tilde{v}_r}{\partial \tilde{z}^2} \tag{16}$$

$$0 \cong -\frac{\partial \tilde{p}}{\partial \tilde{z}} \tag{17}$$

These equations, which are the typical set of expressions proposed for a lubrication flow in a fluid system (Denn, 1980), will be used to describe the flow in the domain between the nozzle and the gauged surface.

2.2. Useful expressions derived from the equations of change

Velocity distributions

The dimensionless velocity component in the *r* direction, $\tilde{v}_r$, can be determined from Eq. (16). Given that the pressure is a function of *r* alone (Eq. (17), *i.e.* $\partial \tilde{p}/\partial \tilde{r} \cong f(\tilde{r})$), and

imposing boundary conditions such as $\tilde{v}_r \cong 0$ at $\tilde{z} = 0$ (gauged surface) and $\tilde{v}_r \cong 0$ at $\tilde{z} = h(\tilde{r})/h_o = \tilde{h}(\tilde{r})$ (nozzle surface), integration of Eq. (16) yields:

$$\tilde{v}_r(\tilde{r},\tilde{z}) \cong \frac{d\tilde{p}}{d\tilde{r}} \frac{\tilde{h}^2}{2} \left[\left(\frac{\tilde{z}}{\tilde{h}} \right)^2 - \frac{\tilde{z}}{\tilde{h}} \right] \tag{18}$$

Note that $\tilde{z}/\tilde{h} < 1$ so $\tilde{v}_r$ is negative. In FDG operation the flow rate through the nozzle is set and/or known. Therefore in order to find the dimensionless pressure gradient in Eq. (18), the following expression for the dimensionless flow rate will be used:

$$\tilde{Q} = \tilde{r} \int_0^{\tilde{h}(\tilde{r})} |\tilde{v}_r| \, d\tilde{z} \tag{19}$$

where $\tilde{Q} = Q / \left[2\pi (r_o - r_i) h_o U_o \right]$ and $|\tilde{v}_r|$ is the absolute value of $\tilde{v}_r$. Incorporating Eq. (18) into Eq. (19) and integrating gives the dimensionless pressure gradient as:

$$\frac{d\tilde{p}}{d\tilde{r}} \cong \frac{12\tilde{Q}}{\tilde{r}\tilde{h}^3} \tag{20}$$

Eq. (18) then becomes:

$$\tilde{v}_r(\tilde{r},\tilde{z}) \cong \frac{6\tilde{Q}}{\tilde{r}\tilde{h}} \left[\left(\frac{\tilde{z}}{\tilde{h}} \right)^2 - \frac{\tilde{z}}{\tilde{h}} \right] \tag{21}$$

The corresponding expression for the *z* component of velocity is obtained by incorporating Eq. (21) into the dimensionless continuity equation (Eq. (15)):

$$\tilde{v}_z(\tilde{r},\tilde{z}) \cong \frac{6\tilde{Q}}{\tilde{r}\tilde{h}} \left(\frac{d\tilde{h}}{d\tilde{r}} \right) \left[\left(\frac{\tilde{z}}{\tilde{h}} \right)^3 - \left(\frac{\tilde{z}}{\tilde{h}} \right)^2 \right] \tag{22}$$

An interesting relationship is obtained by dividing Eqs. (22) and (21):

$$\frac{\tilde{v}_z(\tilde{r},\tilde{z})}{\tilde{v}_r(\tilde{r},\tilde{z})} \cong \frac{\tilde{z}}{\tilde{h}} \frac{d\tilde{h}}{d\tilde{r}} \tag{23}$$

Eq. (23) shows that there will be a non-zero component of velocity in the *z* direction if the nozzle profile is not horizontal.

177

178 *Shear stress on gauged surface*

179 For a Newtonian fluid, the component of the shear stress relevant to the stress on the gauged

180 surface τ_{rz} can be expressed as (Bird *et al*., 2007):

181 $$\tau_{rz} = -\mu\left(\frac{\partial v_r}{\partial z} + \frac{\partial v_z}{\partial r}\right) \tag{24}$$

182 Incorporating the above results, namely (*i*) $V = \varepsilon U_o$; (*ii*) $\varepsilon = h_o/(r_o - r_i)$ gives the

183 dimensionless form:

184 $$\tilde{\tau}_{rz} = -\left(\frac{\partial \tilde{v}_r}{\partial \tilde{z}} + \varepsilon^2 \frac{\partial \tilde{v}_z}{\partial \tilde{r}}\right) \tag{25}$$

185 where: $\tilde{\tau}_{rz} = \tau_{rz}/\left[\mu(U_o/h_o)\right]$.

186

187 Applying the condition $\varepsilon^2 << 1$, Eqs. (21) and (22) in Eq. (25), yields the expression for

188 the dimensionless shear stress evaluated at the gauged surface ($\tilde{z} = 0$):

189 $$\tilde{\tau}_{rz}\big|_{\tilde{z}=0} = \tilde{\tau}_w \cong \frac{6\tilde{Q}}{\tilde{r}\tilde{h}^2} \tag{26}$$

190 It is helpful to introduce a new normalized radial co-ordinate in order to simplify the above

191 results. Defining

192 $$\tilde{r}' = \frac{\tilde{r}}{\tilde{r}_o} = \frac{r}{r_o} \tag{27}$$

193 scales the radial dimension of the domain from 0 to 1. Similarly, the following expressions

194 for the dimensionless shear stress and pressure gradient are introduced so that the variables

195 are only dependent of the geometrical parameters:

196 $$\tilde{\tau}_w^* = \frac{\tilde{\tau}_w (r_o - r_i)}{6 r_o \tilde{Q}} \tag{28}$$

197 $$\frac{d\tilde{p}^*}{d\tilde{r}'} = \frac{\left(d\tilde{p}/d\tilde{r}'\right)}{12\tilde{Q}} \tag{29}$$

198 Equations (20) and (26) can now be expressed as:

199 $$\frac{d\tilde{p}^*}{d\tilde{r}'} \cong \frac{1}{\tilde{r}'\tilde{h}^3} \tag{30}$$

200 $$\tilde{\tau}_w^* \cong \frac{1}{\tilde{r}'\tilde{h}^2} \tag{31}$$

201 Combining Eqs. (30) and (31) gives a useful expression for calculating the wall shear stress:

202 $$\tilde{\tau}_w^* \cong \tilde{h}\left(\frac{d\tilde{p}^*}{d\tilde{r}'}\right) \tag{32}$$

203 Measuring local shear stresses is challenging but it is relatively straightforward to measure
204 local pressure values under the nozzle and therefore the pressure gradient, as reported by
205 Chew *et al*., (2004a) and Peralta *et al*. (2011).

206

207 Equations (30) - (32) are important in considering nozzle geometry because they relate the
208 local shear stress and the pressure gradient to $\tilde{h}$. By specifying the profile of one of $\tilde{h}$, $\tilde{\tau}_w^*$
209 or $d\tilde{p}^*/d\tilde{r}'$, the expressions for the rest of the main parameters (*i.e*. shear stress, pressure
210 gradient, external nozzle geometry, velocity components, *etc*.) can be determined.

211

212 **2.3. Range of Theoretical Validity of the Approach**

213 An important consideration is the ability to verify the range of validity of the solutions.
214 Verification is based on checking whether the main assumptions of the model are met.
215 These assumptions are:

216 $$(i)\ \mathrm{Re}\ \varepsilon = \frac{\rho U_o h_o^2}{\mu\left(r_o - r_i\right)} = \frac{\dot{m} h_o}{2\pi\mu\left(r_o - r_i\right) r_o} = \frac{d\,\mathrm{Re}_d\, h_o}{8\left(r_o - r_i\right) r_o} << 1 \tag{33}$$

217 or, simply

$$\mathrm{Re}_d << \frac{8r_o}{\varepsilon d} \tag{34}$$

where $\mathrm{Re}_d = 4\dot{m}/\pi\mu d$ and

$$(ii)\quad \varepsilon^2 = \frac{h_o^2}{\left(r_o - r_i\right)^2} << 1 \tag{35}$$

It is noteworthy that the above statements represent a sufficient set for checking, because these are less restrictive conditions than those appearing in Eqs. (12) and (14), such as those relating to $\mathrm{Re}\,\varepsilon^p$ ($p > 1$) and ε^n ($n > 2$).

A typical set of parameters from FDG measurements using water as the gauging fluid reported by Chew *et al*. (2004a) are used as an illustration of the approach. The dimensions are h_o = 0.25 mm, r_o = 15 mm, r_i = 5 mm, d = 0.02 m, flow rate ≤ 5 g s^{-1}, giving $\mathrm{Re}_d << 300$ and $\varepsilon^2 = 0.0004$. These conditions guarantee that for low flow rates, the approach presented in this work can be used to describe the FDG system.

3. Materials & Methods

3.1. Case studies

The methodology was tested by proposing simple expressions for one of $\tilde{\tau}_w^*$, $d\tilde{p}^*/d\tilde{r}'$ or $\tilde{h}$ and calculating the solution for the remaining two parameters. The expressions thus obtained were compared with numerical results obtained using CFD simulations. A general type of expression was assigned for each parameter specified:

$$\tilde{f}\left(\tilde{r}'\right) = \frac{f\left(\tilde{r}'\right)}{f\left(1\right)} \tag{36}$$

where $f\left(\tilde{r}'\right)$ is a generic expression for either $\tilde{\tau}_w^*$, $d\tilde{p}^*/d\tilde{r}'$ or $\tilde{h}$, and $f\left(1\right)$ is $f\left(\tilde{r}'\right)$ evaluated at $\tilde{r}' = \tilde{r}_o' = 1$ (outer radius).

240

241 **3.2. CFD simulations**

242 Some of the case study scenarios were evaluated using a commercial CFD code, in a similar
243 manner to previous studies reported by Peralta *et al.* (2011). Briefly, a 2D-axisymmetric
244 computational domain based on that employed by Chew *et al*. (2004a) for modelling quasi-
245 static FDG systems was used. Figure 3 shows a representative computational domain
246 employing cylindrical co-ordinates and the associated boundary conditions.

247

248 The simulations were performed using different values of Re_d. Unless otherwise specified
249 all simulations employed a clearance (closest point between the nozzle and the gauged
250 surface) set at $h/d_t = 0.05$, which lies within the incremental or working zone depicted in
251 Figure 1(*b*).

252

253 The flow at the exit of the domain was assumed to be laminar and fully developed owing to
254 the range of Re_d values used. The governing equations were the Navier-Stokes and
255 continuity equations. The fluid properties were taken as those of water at 20°C.

256

257 The domain was discretised using a triangular mesh. In zones where it was important to
258 estimate the velocity gradients accurately (*e.g.* the gap between the nozzle and the gauged
259 surface) a higher density mesh was used (Figure 3(*b*)). The commercial finite-element-based
260 software COMSOL Multiphysics 3.5a and 4 (COMSOL Ltd., Hatfield, United Kingdom)
261 was used to perform the CFD simulations on a 2.4 GHz desktop PC equipped with 5
262 processors and 4 GB of RAM. Each simulation took about 5 min to converge.

263

The CFD simulations were validated in the previous study (Peralta *et al*., 2011). In brief, the validation consisted of a test of the independency of the studied variables on the mesh configuration and agreement between predicted values with experimental observations. The mesh independency test was carried out using different mesh densities over the entire domain. Monotonic convergence was observed for meshes with > 3,000 elements. The second step was carried out using: (*i*) experimental values of pressure on the gauged surface, and (*ii*) theoretical values of shear stress for selected operating conditions based on the assumption that the flow can be approximated as radial between two parallel disks.

4. Results & Discussion

Table 1 summarises the expressions for the external nozzle geometry, pressure gradient under the nozzle and shear stress on the gauged surface, based on the use of an arbitrary function $\tilde{f}\left(\tilde{r}'\right)$ for one of these variables. The relationships are easy to manipulate. These expressions will be used in the following sections to show some examples for specified nozzle geometry, pressure gradient and shear stress.

4.1. Specified nozzle geometry

4.1.1. Linear nozzle profile

A linear profile is one of the simplest external nozzle geometries to manufacture and analyse. The nozzle shape can be either normal (*i.e.* parallel to the gauged surface), convergent or divergent. For this case, the dimensionless nozzle profile is given by:

$$\tilde{f}_h\left(\tilde{r}'\right) = \tilde{h} = a_h\left(\tilde{r}'-1\right)+1 \tag{37}$$

where a_h is the slope of the linear profile of the external nozzle geometry. Working from the first row in Table 1, expressions for the pressure gradient and shear stress are:

288 $$\frac{d\tilde{p}^*}{d\tilde{r}'} \cong \frac{1}{\tilde{r}'\left[a_h\left(\tilde{r}'-1\right)+1\right]^3} \tag{38}$$

289 $$\tilde{\tau}_w^* \cong \frac{1}{\tilde{r}'\left[a_h\left(\tilde{r}'-1\right)+1\right]^2} \tag{39}$$

290 Fig. 4 shows the functionality obtained for a linear profile of $\tilde{h}$ (Fig 4(*a*)) for different and
291 representative values of a_h. The $\tilde{\tau}_w^*$ profiles in (Fig. 4(*c*)) show a marked decrease as $\tilde{r}'$
292 increases for positive values of a_h which is accentuated at higher a_h. With negative a_h, the
293 $\tilde{\tau}_w^*$ profiles still present a concave shape but with a minimum within the nozzle region. This
294 feature is discussed in detail in Section 4.1.1.1.
295
296 The pressure profiles in Fig. 4(*d*) were obtained by integrating the gradients in Fig. 4(*b*):

297 $$-\tilde{p}^* \cong -\frac{a_h\left(\tilde{r}'-1\right)\left\{a_h-1+\left(a_h-3\right)\left[a_h\left(\tilde{r}'-1\right)+1\right]\right\}}{2\left[a_h\left(\tilde{r}'-1\right)+1\right]^2\left(a_h-1\right)^2} - \frac{1}{\left(a_h-1\right)^3}\ln\left[\frac{a_h\left(\tilde{r}'-1\right)+1}{\tilde{r}'}\right] - \tilde{p}_o^* \tag{40}$$

298 Figure 4(*d*) shows a change in the profiles from convex to concave as a_h changes from
299 positive to negative values. This follows the change in the nozzle shape from a converging
300 to a diverging one. As a_h becomes more positive, the external part of the nozzle becomes
301 more convergent, concentrating the pressure drop near the inner radius of the nozzle.
302 Conversely, highly negative a_h values concentrate the pressure loss near the outer rim of
303 the nozzle. The same information can be extracted from the pressure gradient (Fig. 4(*b*)).
304
305 Finally, it is noteworthy that when $a_h = 0$, Eq. (40) reduces to the expression for the radial
306 flow between two parallel disks (Middleman, 1998):

307 $$-\tilde{p}^* \cong -\ln(\tilde{r}') - \tilde{p}_o^* \quad (41)$$

308 An important parameter to quantify is the area-averaged shear stress on the gauged surface,
309 as this can be related to material properties when the nozzle deforms the film $\langle \tilde{\tau}_w^* \rangle$. This is
310 defined as:

311 $$\langle \tilde{\tau}_w^* \rangle = \frac{2}{\left(1-\tilde{r}_i'^2\right)} \int_{\tilde{r}_i'}^{1} \tilde{\tau}_w^* \, \tilde{r}' \, d\tilde{r}' \quad (42)$$

312 where $\langle \tilde{\tau}_w^* \rangle = \langle \tau_w \rangle / \tau_o$, and $\tau_o = 3\mu\dot{m}/\left(\pi\rho h_o^2 r_o\right) : \tau_o$ is the shear stress calculated for radial
313 flow between parallel disks with separation h_o, evaluated at r_o (Middleman, 1998).
314 Introducing Eq. (39) into Eq. (42), gives:

315 $$\langle \tilde{\tau}_w^* \rangle \cong \frac{2}{(1+\tilde{r}_i')[a_h(\tilde{r}_i'-1)+1]} \quad (43)$$

316 Figure 5(*a*) shows that the average shear stress $\langle \tilde{\tau}_w^* \rangle$ increases with Re_d: it should be noted
317 that these results were all calculated for a fixed clearance, as varying the clearance for a
318 given flow rate will also change Re_d and $\langle \tilde{\tau}_w^* \rangle$. The effect of nozzle shape on the averaged
319 shear stress is stronger when $a_h > 0$, *i.e.* convergent nozzles, as the position where the
320 nozzle approaches the film most closely is where the circumferential area is also a
321 minimum.
322
323 Figure 5(*b*) summarises the effect of nozzle width in terms of $\langle \tilde{\tau}_w^* \rangle$, the area-averaged shear
324 stress divided by τ_o. When $\tilde{r}_i' = 1$, the width is negligible. The plots show that
325 $\langle \tilde{\tau}_w^* \rangle$ increases with nozzle width when a_h is positive. When $a_h < 0$ $\langle \tilde{\tau}_w^* \rangle$ is ≤ 1 and at
326 certain values of $\tilde{r}_i'$ there is a minimum in $\langle \tilde{\tau}_w^* \rangle$, located at

$$\tilde{r}_i' \cong -\frac{1}{2a_h} \tag{44}$$

Minima are obtained for $a_h \leq -0.5$. The existence of minimum values of $\left\langle \tilde{\tau}_w^* \right\rangle$ is of interest for measuring deposit thicknesses, where a low shear stress is advantageous in order to avoid deforming the deposit. When comparing the reduction in $\left\langle \tilde{\tau}_w^* \right\rangle$ for a nozzle with $\tilde{r}_i'$ given by Eq. (44), a suitable reference value is that evaluated at $\tilde{r}_i' = 0$ (denoted $\left\langle \tilde{\tau}_w^* \right\rangle_{\tilde{r}_i'=0}$). Introducing Eq. (44) into Eq. (43) and dividing by $\left\langle \tilde{\tau}_w^* \right\rangle_{\tilde{r}_i'=0}$ gives

$$\frac{\left\langle \tilde{\tau}_w^* \right\rangle_{\min}}{\left\langle \tilde{\tau}_w^* \right\rangle_{\tilde{r}_i'=0}} \cong -\frac{4a_h(1-a_h)}{(2a_h-1)^2} \tag{45}$$

Figure 6 shows the results computed for $a_h \leq -0.5$. The reduction in shear stress by using the minimum area-averaged shear stress exhibits a maximum at $\tilde{r}_i' = 0.5$ (Fig. 6(*b*)). The plots show that the reduction in $\left\langle \tilde{\tau}_w^* \right\rangle$ can be in the order of 10% if the inner radius of the nozzle is made as small as possible.

4.1.1.1. The 'saddle profile' case

Peralta *et al*. (2011) demonstrated that a mildly divergent nozzle with a linear external surface profile and angle of approximately -5° gave a shear stress profile with two peaks of the same magnitude located at the positions of the inner and outer rim. This is termed a 'saddle profile' and is considered further using the approach presented above. For this case, (a_h) can be related to the angle (θ) by

$$a_h = \frac{r_o}{h_o} \tan\left(\frac{\pi\theta}{180}\right) \tag{46}$$

and the shear stress profile on the gauged surface is estimated as:

347 $$\tilde{\tau}_w^* \cong \frac{1}{\left(\frac{r}{r_o}\right)\left[\frac{r_o}{h_o}\tan\left(\frac{\pi\theta}{180}\right)\left(\frac{r}{r_o}-1\right)+1\right]^2} \quad (47)$$

348 Evaluating Eq. (47) at r_i and assuming that $\tilde{\tau}_w^* \cong 1$ (*i.e.* a peak at r_i), gives the following

349 expression for the angle that will produce a saddle profile, θ_{sp}:

350 $$\theta_{\text{sp}} \cong \frac{180}{\pi}\arctan\left[\frac{h_o}{(r_o-r_i)}\left(1-\sqrt{\frac{r_o}{r_i}}\right)\right] \quad (48)$$

351 Expressing the *tan* function as an infinite series (Bronshtein *et al*., 2007) and recalling that

352 its argument is small (because $\varepsilon << 1$), gives:

353 $$\theta_{\text{sp}} \cong \frac{180}{\pi}\frac{h_o}{(r_o-r_i)}\left(1-\sqrt{\frac{r_o}{r_i}}\right) \quad (49)$$

354 Eq. (49) indicates that θ_{sp} is (*i*) negative; (*ii*) proportional to h_o; (*iii*) independent of the

355 flow conditions, and (*iv*) dependent on r_o and r_i, that is, the size of the nozzle.

356

357 The distribution of shear stress on the gauged surface for selected values θ_{sp} is compared

358 with CFD simulations in Figure 7(*a*). The profiles exhibit two peaks, as expected, with very

359 good agreement in magnitudes and locations of the peaks.

360

361 Figure 7(*b*) shows the dimensionless shear stress values evaluated at $\tilde{r}_i'$ (the inner radius of

362 the nozzle) as a function of the slope angle of the nozzle rim, for different values of

363 clearance, h_o. θ_{sp} corresponds to the angle where $\tilde{\tau}_w^*\big|_{\tilde{r}_i'} = 1$, and becomes more negative as

364 h_o increases. The $\tilde{\tau}_w^*\big|_{\tilde{r}_i'}$ profiles show a strong dependency on h_o, which varies with the

365 nozzle angle. The strong dependence of $\tilde{\tau}_w^*\big|_{\tilde{r}_i'}$ on θ in the range close to θ_{sp} was also

366 observed by Peralta *et al*. (2011). These results indicate that the desired effect, of a shear

367 stress distribution close to uniform, is only achievable with a narrow range of operating
368 conditions for a given nozzle, so that alternative geometries should be investigated.
369
370 *4.1.2. Non-linear nozzle profiles*
371 The flexibility of modern fabrication techniques means that there are few limits on the
372 shapes available for FDG nozzles. Some geometries are easier to manufacture than others,
373 two examples being toroidal and parabolic-toroidal profiles (Figure 8). The non-dimensional
374 expressions for these profiles are:

375 $$\tilde{h} = 1 - \sqrt{(\tilde{r}' - \tilde{r}_i')(1 - \tilde{r}')} \qquad \text{(toroidal)} \qquad (50)$$

376 $$\tilde{h} = \frac{4\left(1 - \tilde{h}_m\right)}{\left(1 - \tilde{r}_i'\right)^2}\left[\tilde{r}'^2 - (1 + \tilde{r}_i')\tilde{r}' + \tilde{r}_i'\right] + 1 \qquad \text{(parabolic-toroidal)} \qquad (51)$$

377 where $\tilde{h}_m$ is the value of $\tilde{h}$ at the position of the minimum distance between the nozzle and
378 the gauged surface. The shear stress profiles evaluated for the above geometries are
379 compared with CFD simulations in Figure 8 for a representative set of operating conditions.
380 Good agreement is obtained, supporting the use of the analytical approach.
381
382 **4.2. Specified pressure gradient**
383 The simplest profile that represents also an interesting scenario is that of a linear variation in
384 pressure gradient. The pressure gradient is written as

385 $$\tilde{f}_{pg}\left(\tilde{r}'\right) = \frac{d\tilde{p}^*}{d\tilde{r}'} = a_{pg}\left(\tilde{r}' - 1\right) + 1 \qquad (52)$$

386 where a_{pg} is the slope. From Table 1, the following expressions for the external nozzle
387 profile and the shear stress on the gauged surface are obtained:

388 $$\tilde{h} \cong \frac{1}{\sqrt[3]{\tilde{r}'\left[a_{pg}\left(\tilde{r}' - 1\right) + 1\right]}} \qquad (53)$$

389 $$\tilde{\tau}_w^* \cong \sqrt[3]{\frac{\left[a_{pg}\left(\tilde{r}'-1\right)+1\right]^2}{\tilde{r}'}} \qquad (54)$$

390 Figure 9 shows the profiles for each parameter for different and representative values of
391 a_{pg}. In general, the uniform pressure gradient requires $\tilde{h}$ to decrease as $\tilde{r}'$ increases for
392 $a_{pg} \le 0$, and this effect is accentuated as a_{pg} becomes more negative. This behaviour
393 persists even for $a_{pg} > 0$. For some positive values of a_{pg}, a minimum is observed in $\tilde{h}$.
394 When $a_{pg} \cong 1$, the profile changes from convex to concave with a minimum near $\tilde{r}' = 0$.

395

396 The corresponding shear stress profiles in Fig. 9(*b*) show increasing $\tilde{\tau}_w^*$ values as $\tilde{r}'$
397 decreases for $a_{pg} \ge 0$, and a minimum when $a_{pg} < 0$. The presence of the minimum
398 indicates that a saddle profile (in terms of shear stress on the gauged surface) can be
399 obtained in this case. The figure also shows that a convex type of profile can be expected for
400 both positive and negatives values of a_{pg}.

401

402 The pressure profiles in Figure 9(*c*) were evaluated using

403 $$-\tilde{p}^* \cong \frac{a_{pg}}{2}\left(1-\tilde{r}'^2\right)+\left(1-a_{pg}\right)\left(1-\tilde{r}'\right)-\tilde{p}_o^* \qquad (55)$$

404 The plots show a change in the profiles from concave to convex when a_{pg} changes from
405 positive to negative. The pressure values in this case are lower than those in the previous
406 section because the gradients are linear.

407

408 The area-averaged shear stress can be calculated, as in the case for linear $\tilde{h}$, using Eqs. (42)
409 and (54), *viz*.

$$\left\langle \tilde{\tau}_w^* \right\rangle \cong \frac{2}{\left(1-\tilde{r}_i'^2\right)}\left\{\frac{3}{14a_{pg}}\left[1+a_{pg}-\left(1-a_{pg}\right){}_2F_1\left(1,\frac{4}{3};\frac{5}{3};\frac{a_{pg}}{a_{pg}-1}\right)\right]\right.$$

410
$$-\frac{3}{14a_{pg}}\left\{\tilde{r}_i'\left[a_{pg}\left(\tilde{r}_i'-1\right)+1\right]\right\}^{2/3}$$

$$\left.\left[1+a_{pg}\left(2\tilde{r}_i'-1\right)+\left(1-a_{pg}\right){}_2F_1\left(1,\frac{4}{3};\frac{5}{3};\frac{a_{pg}}{a_{pg}-1}\tilde{r}_i'\right)\right]\right\} \qquad (56)$$

411 where ${}_2F_1\left[a,b;c;x\right]$ is the Gauss hypergeometric function (Gasper and Rahman, 2004). The
412 dependence of $\left\langle \tilde{\tau}_w^* \right\rangle$ on Re_d and $\tilde{r}_i'$ is plotted in Figure 10. The profiles exhibit a stronger
413 effect of Re_d on $\left\langle \tilde{\tau}_w^* \right\rangle$ compared with Figure 5 ($\tilde{h}$ linear) for a particular $\tilde{r}_i'$ value and the
414 reduced sensitivity of $\left\langle \tilde{\tau}_w^* \right\rangle$ to the magnitude of a_{pg} values as $\tilde{r}_i'$ is decreased.

415

416 *4.2.1. Linear pressure profile:* $d\tilde{p}^*/d\tilde{r}'=1,\ a_{pg}=0$

417 A second case of interest is where the pressure varies linearly across the nozzle rim, *i.e.*
418 $a_{pg}=0$ and Eq. (52) gives $d\tilde{p}^*/d\tilde{r}'=1$. The dimensional pressure profile evaluated at the
419 gauged surface ($z=0$) is then given by:

420
$$-p \cong \frac{3\mu^2 d\,\mathrm{Re}_d}{2\rho h_o^3}\left(1-\frac{r}{r_o}\right)-p_o \qquad (57)$$

421 where p_o is the pressure at r_o. Comparisons between Eq. (57) and CFD simulations for
422 different values of Re_d in Figure 11 show very good agreement up to $\mathrm{Re}_d \cong 40$. At the
423 highest Re_d value considered, $\mathrm{Re}_d=60$, the mean percentage error was around 6.64%.

424

425 **4.3. Specified shear stress profile**

426 The scenario where the shear stress on the gauged surface varies linearly is now considered.
427 The basis function is:

$$\tilde{f}_s(\tilde{r}') = \tilde{\tau}_w^* = a_s(\tilde{r}'-1)+1 \tag{58}$$

where a_s is the gradient in the shear stress profile. The corresponding forms for the nozzle shape and pressure gradient are:

$$\tilde{h} \cong \frac{1}{\sqrt{\tilde{r}'\left[a_s(\tilde{r}'-1)+1\right]}} \tag{59}$$

$$\frac{d\tilde{p}^*}{d\tilde{r}'} \cong \sqrt{\tilde{r}'\left[a_s(\tilde{r}'-1)+1\right]^3} \tag{60}$$

The loci for each parameter evaluated for different and representative values of a_s are presented in Figure 12. Figure 12(*c*) shows that $\tilde{h}$ decreases as $\tilde{r}'$ increases for $a_s > 0$, corresponding to a recessed nozzle with the point of closest approach to the layer located at the outer rim. When $a_s < 0$, there is a minimum in $\tilde{h}$ as $\tilde{r}'$ increases. The pressure gradient profiles in Fig. 12(*d*) show strongly non-linear behaviour and are more sensitive to a_s. The corresponding pressure profiles are all monotonic in a_s, given by

$$-\tilde{p}^* \cong \frac{2}{3}(1-a_s)^{3/2}\left[{}_2F_1\left(-\frac{3}{2},\frac{3}{2};\frac{5}{2};\frac{a_s}{a_s-1}\right)-\tilde{r}'^{3/2}\,{}_2F_1\left(-\frac{3}{2},\frac{3}{2};\frac{5}{2};\frac{a_s\tilde{r}'}{a_s-1}\right)\right]-\tilde{p}_o^* \tag{61}$$

where ${}_2F_1[a,b;c;x]$ is the Gauss hypergeometric function (Gasper and Rahman, 2004).

Constant $\tilde{\tau}_w^*$

A special case of Eq. (61) arises when $a_s = 0$ and the shear stress on the surface being studied is uniform. This scenario is desirable for FDG measurements of deposit strength or deformation. A number of scenarios were evaluated and compared with CFD simulations. Figure 13 shows a comparison with CFD and analytical predictions of pressure and shear stress on the gauged surface for different values of Re_d, where the local pressure is given by Eq. (61), in dimensional form:

449 $$-p \cong \frac{\mu^2 d\,\mathrm{Re}_d}{\rho h_o^3}\left[1-\left(\frac{r}{r_o}\right)^{3/2}\right]-p_o \qquad (62)$$

450 Figure 13(*a*) shows that the agreement was good in all cases, with a mean percentage error <
451 6%. Absolute pressures are considered here as these can be measured with reasonable
452 accuracy for verification purposes. Fig. 13(*b-d*) shows the corresponding shear stress
453 profiles: the simulations agree with Eq. (58) well underneath the nozzle lip, with a peak at
454 the inner and outer rim locations.

455

456 Finally, the area-averaged shear stress is given by:

457 $$\left\langle \tilde{\tau}_w^* \right\rangle \cong \frac{2a_s\left(1-\tilde{r}_i'^3\right)}{3\left(1-\tilde{r}_i'^2\right)}-a_s+1 \qquad (63)$$

458 The effect of Re_d and $\tilde{r}_i'$ on $\left\langle \tilde{\tau}_w^* \right\rangle$ summarized in Figure 14 shows similar behaviour to the
459 results obtained for linear $d\tilde{p}^*/d\tilde{r}'$.

460

461 **4.4. Composite nozzles**

462 The analytical expressions developed here can be used to investigate potential combinations
463 of features. For example, the nozzle shape could be specified to exploit two aspects of FDG
464 action, one of which is sensitive to nozzle shape near the inner rim and a second which is
465 sensitive to shape near the outer rim. By way of example, Figure 15 shows a nozzle
466 geometry with an outer zone of constant $\tilde{h}$ and an inner zone with constant $\tilde{\tau}_w^*$. The Figure
467 also shows good agreement between the dimensional shear stress calculated for a particular
468 Re_d and the composite, analytical model. This nozzle affords better sensitivity to clearance
469 (data not shown), important in locating the surface in thickness measurements, and a
470 reasonably uniform shear stress. The scope for designing nozzles for particular applications

471 is therefore demonstrated. In these combinations, it is important to note that Eqs. (34) and
472 (35) must hold for the individual simpler systems.
473
474 **5. Conclusions**
475 An analysis of the flow pattern under the gauging nozzle has been developed using the
476 lubrication approximation to obtain expressions for the main flow variables in an FDG
477 experiment. A set of general equations for the external nozzle geometry, pressure gradient
478 under the nozzle and shear stress on the gauged surface were obtained. Case studies were
479 presented considering the simple or common scenarios (*i.e.* linear profiles of all variables
480 studied). Computational fluid dynamics simulations were used to validate the model using
481 representative cases and showed good agreement. The range of applicability of the
482 expressions lay in the range estimated by the model.
483
484 These results not only provide a tool to investigate the effect of the external nozzle
485 geometry on parameters affecting the surface being studied by the FDG technique, in
486 *design*, but also allow the effect of changes on operating variables on the performance of an
487 existing FDG nozzle to be evaluated, *i.e.* assessing *operability*. The tools allow initial
488 configurations of nozzle shape for specified operating conditions to be identified, for
489 optimization by CFD simulations and eventually *in vivo* by experiments.
490
491 Further developments could include extension of the analysis for systems with higher
492 Reynolds numbers (*i.e.* significant inertial effects), non-Newtonian fluids, and porous
493 surfaces (*e.g.* membranes).
494
495

References

Bird, R.B., Stewart, W.E., Lightfoot, E.N., 2007. Transport Phenomena, second ed. John Wiley & Sons, Inc., New York, USA.

Bronshtein, I. N., Semendyayev, K. A., Musiol, G., Muehlig, H. Handbook of mathematics. 5th Ed. Springer-Verlag. Berlin. Germany.

Chew, Y. M. J., Cardoso, S. S. S., Paterson, W. R., Wilson, D. I. 2004b. CFD studies of dynamic gauging. Chemical Engineering Science 59(16), 3381–3398.

Chew, Y. M. J., Höfling, V., Augustin, W., Paterson, W. R., Wilson, D. I. 2005. A method for measuring the strength of scale deposits on heat transfer surfaces. Developments in Chemical Engineering and Mineral Processing 13(1-2), 21-30.

Chew, Y. M. J., Paterson, W. R., Wilson, D. I. 2004a. Fluid dynamic gauging for measuring the strength of soft deposits. Journal of Food Engineering 65(2), 175–187.

Denn, M. 1980. Process Fluid Mechanics. Prentice-Hall, London, UK.

Gasper, G., Rahman, M. 2004. Basic hypergeometric series. Cambridge University Press. Cambridge. U.K.

Gordon, P. W. Brooker, A. D. M., Chew, Y. M. J., Wilson, D. I., York, D. W. 2010. A scanning fluid dynamic gauging technique for probing surface layers. Measurement Science and Technology 21(8), art number: 085103.

Gu, T., Albert, F., Augustin, W., Chew, Y. M. J., Mayer, M., Paterson, W. R., Scholl, S., Sheikh, I., Wang, K., Wilson, D. I. 2011. Application of fluid dynamic gauging to annular test apparatuses for studying fouling and cleaning. Experimental Thermal and Fluid Science 35(3), 509-520.

Gu, T., Chew, Y. M. J., Paterson, W. R., Wilson, D. I. 2009. Experimental and CFD studies of fluid dynamic gauging in duct flows. Chemical Engineering Science 64(2), 219-227.

Lister, V. Y., Lucas, C., Gordon, P. W., Chew, Y. M. J., Wilson, D. I. 2011. Pressure mode fluid dynamic gauging for studying cake build-up in cross-flow microfiltration. Journal of Membrane Science 366(1-2), 304-313.

Middleman, S. 1998. An Introduction to Fluid Dynamics. Principles of Analysis and Design. John Wiley & Sons. New York.

Peralta, J. M., Chew, Y. M. J., Wilson, D. I. 2011. Effect of the nozzle external geometry on the pressure and shear stress exerted on the surface being gauged in fluid dynamic gauging. Sent for publication.

Tuladhar, T. R., Paterson, W. R., Macleod, N., Wilson, D. I. 2000. Development of a novel non-contact proximity gauge for thickness measurement of soft deposits and its application in fouling studies. Canadian Journal of Chemical Engineering 78(5), 935–947.

Nomenclature

a_i	parameter of Eqs. (37), (52) and (58), $i = h, pg, s$.
d	diameter of the tube, m
d_t	nozzle throat diameter, m
f_i	radial profile function for specified variable, $i = h, pg, s$.
g_z	standard gravity in z direction (-9.81), m s^{-2}
h	clearance between the nozzle and the gauged surface, m
h_{init}	position of the nozzle relative to the substrate, m
$\tilde{h}$	dimensionless clearance (h/h_o)
$\tilde{h}_m$	minimum dimensionless clearance
$\dot{m}$	mass flow rate, kg s^{-1}
p	pressure, Pa
$\tilde{p}$	dimensionless pressure defined by Eq. (8)
Q	flow rate, m^3 s^{-1}
$\tilde{Q}$	dimensionless flow rate ($Q/\left[2\pi\left(r_o - r_i\right)h_o U_o\right]$)
r	radial position, m
$\tilde{r}$	dimensionless radial position defined by Eq. (4)
$\tilde{r}'$	dimensionless radial position defined in Eq. (27)
R	radius of the tube, m
Re	Reynolds number ($\rho U_o h_o / \mu$)
Re_d	Reynolds number based on d
U_o	mean fluid velocity at the external radius calculated from the flow rate, m s^{-1}
v_r	velocity component in r direction, m s^{-1}
v_z	velocity component in z direction, m s^{-1}
$\tilde{v}_r$	dimensionless velocity component in r direction defined by Eq. (6)
$\tilde{v}_z$	dimensionless velocity component in z direction defined by Eq. (7)
w	length of the nozzle rim, m
z	axial position, m
$\tilde{z}$	dimensionless axial position defined by Eq. (5)

Greek symbols

α	angle of the internal divergent zone of the nozzle, deg
δ	thickness of the deposit, m
ε	dimensional relation ($h_o/(r_o - r_i)$)
φ	azimuthal co-ordinate, -
θ	angle of the external surface of the nozzle, -
θ_{sp}	angle of the external surface of the nozzle that gives a saddle shear stress profile, -
λ	length of nozzle exit, m
μ	dynamic viscosity, Pa
Π	characteristic pressure, defined as $\Pi = \mu U_o /(h\varepsilon_o)$, Pa
ρ	density, kg m^{-3}
τ	shear stress, Pa
$\tilde{\tau}$	dimensionless shear stress ($\tau/[\mu(U_o/h_o)]$)
$\tilde{\tau}^*$	dimensionless shear stress defined in Eq. (28)

Subscripts

o	at the outer extreme of the nozzle
i	at the inner extreme of the nozzle
w	at the gauged surface

Acknowledgments

JMP wishes to acknowledge Drs Susana Zorrilla and Amelia Rubiolo for their invaluable support during his postdoctoral visit to group at Cambridge, and financial support from the Consejo Nacional de Investigaciones Científicas y Técnicas (CONICET) and Universidad Nacional del Litoral of Argentina. A Royal Academy of Engineering/EPSRC Research Fellowship for YMJC is gratefully acknowledged.

Figure captions

Figure 1. Fluid dynamic gauging principles. (*a*) Schematic of nozzle, with inset showing key dimensions; (*b*) calibration curves showing relationship between mass flow rate, $\dot{m}$, and dimensionless clearance, h/d_t.

Figure 2. Schematic of the physical domain investigated in this work.

Figure 3. Simulation geometry (*a*) showing boundary conditions and domain dimensions, and (*b*) mesh used (a high mesh density is employed under the nozzle rim, in the throat, and along the base).

Figure 4. Dimensionless profiles of (*a*): nozzle external geometry ($\tilde{h}$), (*b*): pressure gradient ($d\tilde{p}^*/d\tilde{r}'$), (*c*) shear stress ($\tilde{\tau}_w^*$), and (*d*) pressure ($-\tilde{p}^*$) as a function of the dimensionless radial position ($\tilde{r}'$) for different values of a_h, for the linear nozzle shape.

Figure 5. (*a*) Effect of Re_d on area-averaged shear stress $\langle \tau_w \rangle$ and (*b*) dimensionless area-averaged shear stress $\langle \tilde{\tau}_w^* \rangle$ as a function of $\tilde{r}_i'$, for different values of a_h for the case of linear nozzle shape.

Figure 6. (*a*) Dimensionless area-averaged shear stress $\langle \tilde{\tau}_w^* \rangle$ as a function of $\tilde{r}_i'$ for selected negative values of a_h showing the existence of a minimum $\langle \tilde{\tau}_w^* \rangle_{\min}$: loci of minima denoted by the dashed line. (*b*) Evaluation of Eq. (45) showing the effect of a_h on loci position and magnitude.

Figure 7. (*a*) Comparison of theoretical (Eq. (47), solid loci) and CFD simulated (dashed loci) dimensionless shear stress $\tilde{\tau}_w^*$ profiles for selected values of θ_{sp}. (*b*) Dimensionless shear stress evaluated at the inner radius of the nozzle ($\tilde{r}_i'$) as a function of the angle of the nozzle rim for different values of h_o.

Figure 8. Comparison between shear stress profiles obtained analytically (solid loci) and from CFD simulations (dashed loci) for (*a*) toroidal nozzle, (Eq. (50)) and (*b*) parabolic-toroidal profile of $\tilde{h}$ ((Eq. (51)). CFD conditions: $\mathrm{Re}_d = 10$, h_o = 0.25 mm, r_i = 2.5 mm and r_o = 15 mm.

Figure 9. Dimensionless profiles of (*a*): pressure gradient ($d\tilde{p}^*/d\tilde{r}'$), (*b*) shear stress ($\tilde{\tau}_w^*$), (*c*) pressure ($-\tilde{p}^*$), and (*d*): nozzle external geometry ($\tilde{h}$) as a function of the dimensionless radial position ($\tilde{r}'$) for different values of a_{pg}, for the case of linear pressure gradient profile.

Figure 10. (*a*) Effect of Re_d on area-averaged shear stress $\langle \tau_w \rangle$ and (*b*) dimensionless area-averaged shear stress $\langle \tilde{\tau}_w^* \rangle$ as a function of $\tilde{r}_i'$, for different values of a_{pg} for the linear pressure gradient profile case.

Figure 11. Comparison between theoretical (Eq. 57, solid loci) and CFD simulation (symbols) of pressure as a function of $\tilde{r}'$ for different Re_d for the case of a linear pressure profile. Symbols: (◊) Re_d = 1, (◊) Re_d = 5, (◊) Re_d = 10, (◊) Re_d = 20, (×) Re_d = 40, and (+) Re_d = 60. For each simulation: h_o = 0.25 mm, r_i = 2.5 mm and r_o = 15 mm.

Figure 12. Dimensionless profiles of (*a*) shear stress ($\tilde{\tau}_w^*$), (*b*) pressure ($-\tilde{p}^*$), (*c*): nozzle external geometry ($\tilde{h}$), and (*d*): pressure gradient ($d\tilde{p}^*/d\tilde{r}'$) as a function of the dimensionless radial position ($\tilde{r}'$) for different values of a_s, for the case of linear shear stress profile.

Figure 13. Comparison between CFD simulation (dashed loci) and analytical predictions (solid loci) of (*a*) pressure with $a_h = 0$ (Eq. 62) and shear stress values (Eq. (58)), for (*b*) $a_h = -0.7$, (*c*) and (*d*) $a_h = 0.25$, as a function of $\tilde{r}'$ for different Re_d. Conditions: h_o = 0.25 mm, r_i = 2.5 mm and r_o = 15 mm.

Figure 14. (*a*) Effect of Re_d on area-averaged shear stress $\langle \tau_w \rangle$ and (*b*) dimensionless area-averaged shear stress $\langle \tilde{\tau}_w^* \rangle$ as a function of $\tilde{r}_i'$, for different values of a_s for the linear shear stress profile case.

Figure 15. Shear stress values as a function of $\tilde{r}'$ for the example of a composite nozzle with constant $\tilde{h}$ at the outer part of the nozzle and constant $\tilde{\tau}_w^*$ at the inner part (Re_d = 10, h_o = 0.25 mm). Loci show the analytical model predictions and circles the values obtained from CFD simulation.

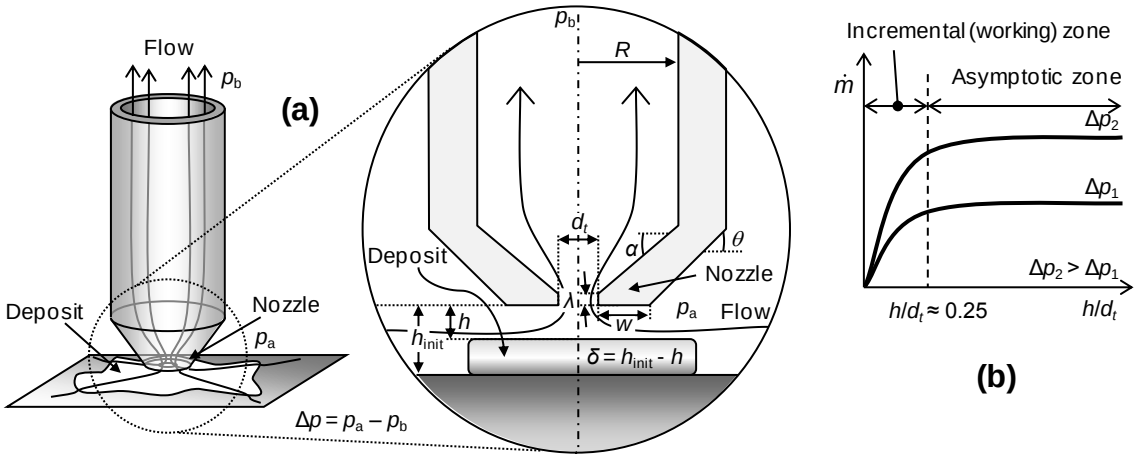

656

657

658 **Figure 1.** Fluid dynamic gauging principles. (*a*) Schematic of nozzle, with inset showing
659 key dimensions; (*b*) calibration curves showing relationship between mass flow rate, $\dot{m}$,
660 and dimensionless clearance, h/d_t.

661

662

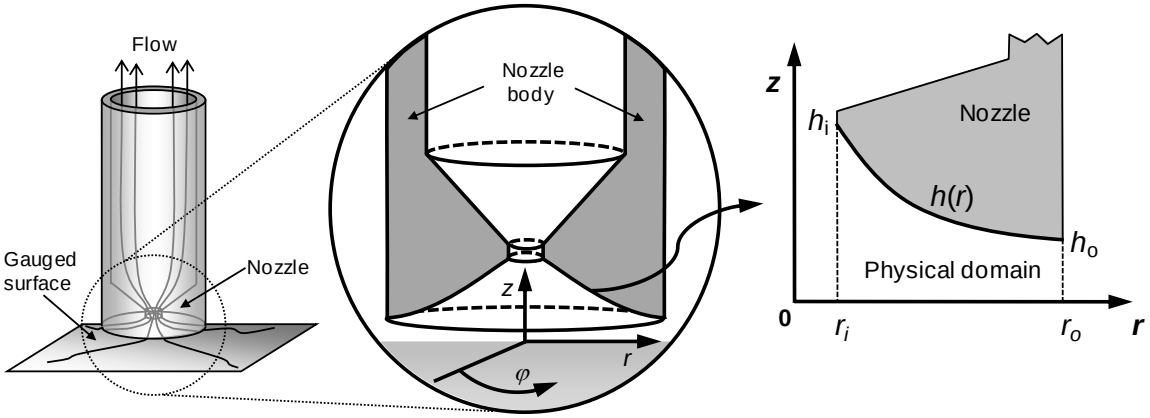

663

664

665 **Figure 2.** Schematic of the physical domain investigated in this work.

666

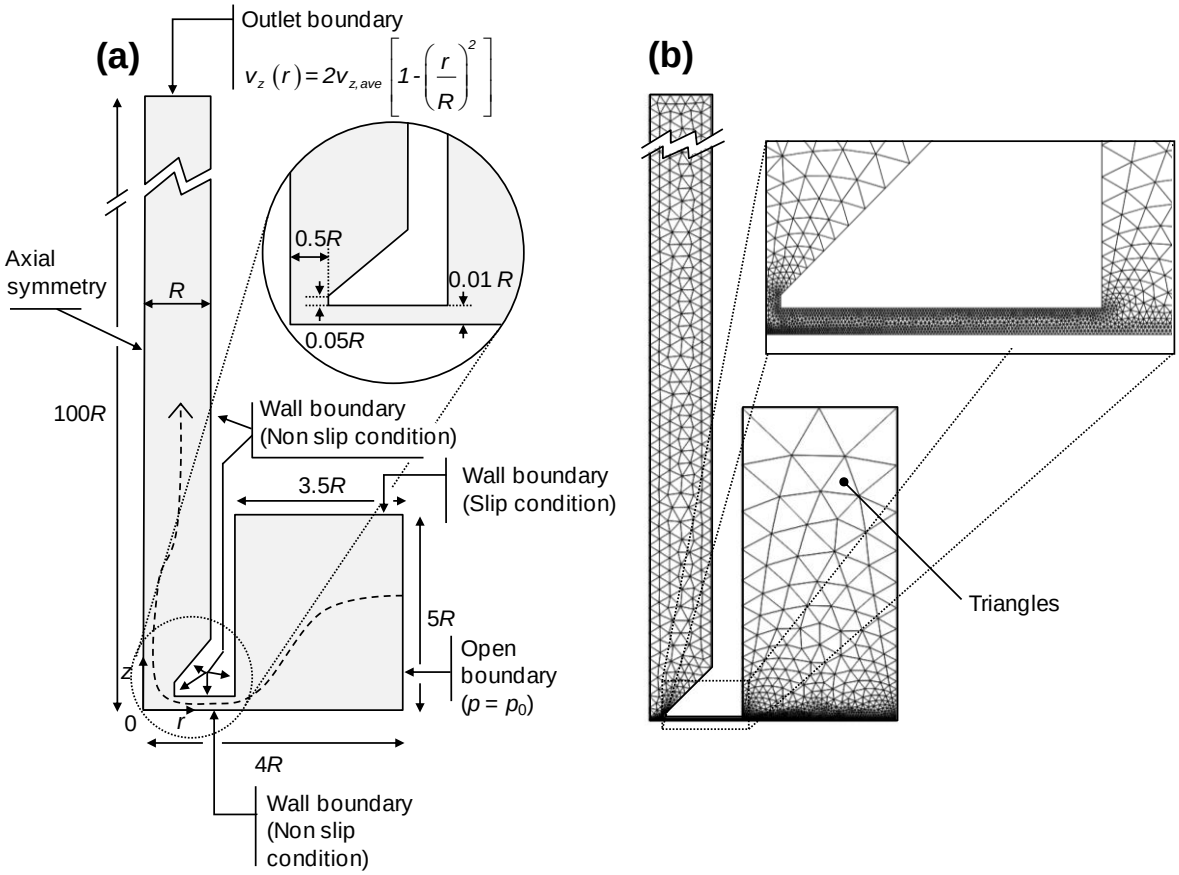

667

668

669 **Figure 3.** Simulation geometry (*a*) showing boundary conditions and domain dimensions,
670 and (*b*) mesh used (a high mesh density is employed under the nozzle rim, in the throat, and
671 along the base).

672

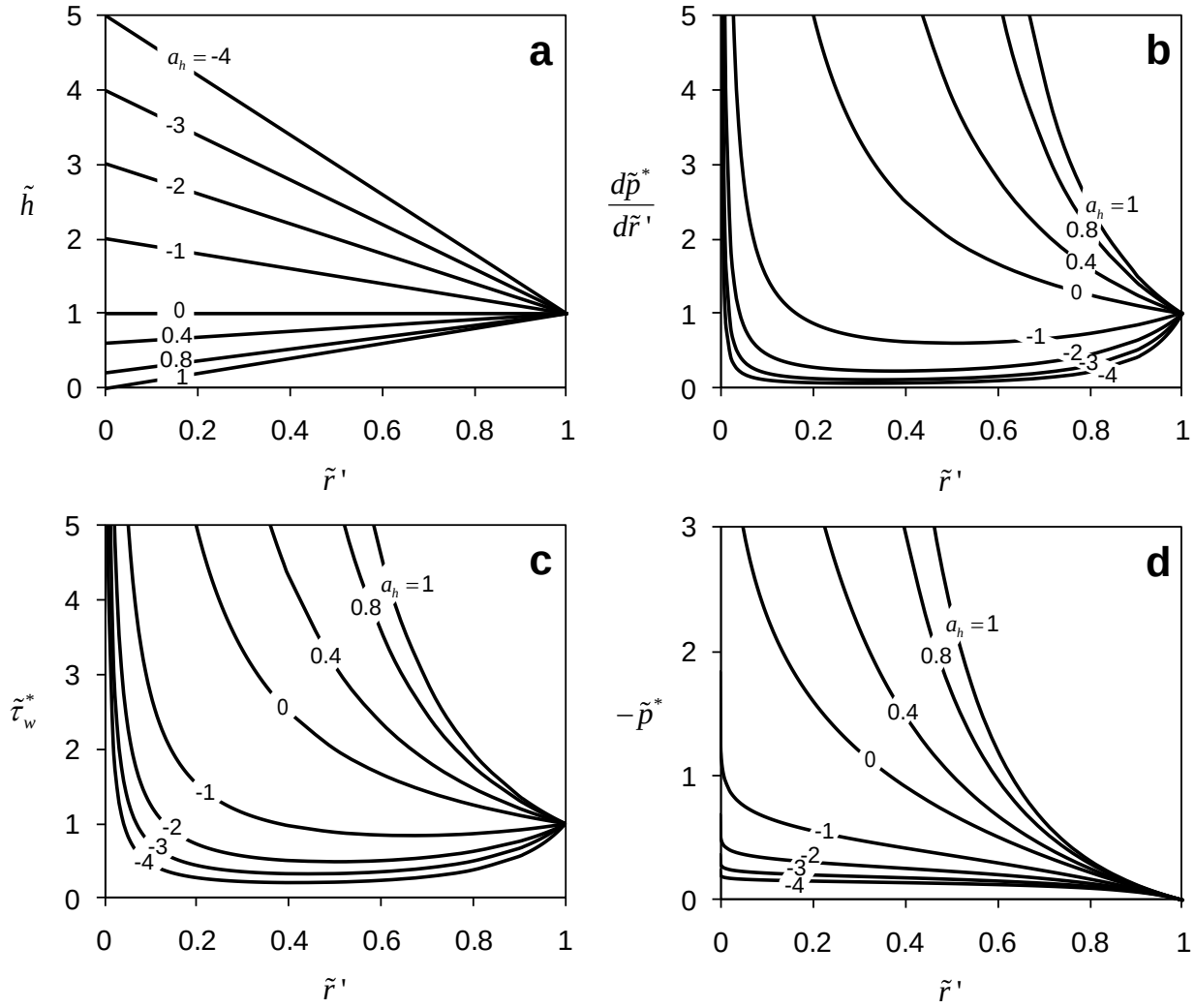

673

674

675 **Figure 4.** Dimensionless profiles of (*a*): nozzle external geometry ($\tilde{h}$), (*b*): pressure
676 gradient ($d\tilde{p}^*/d\tilde{r}'$), (*c*) shear stress ($\tilde{\tau}_w^*$), and (*d*) pressure ($-\tilde{p}^*$) as a function of the
677 dimensionless radial position ($\tilde{r}'$) for different values of a_h, for the linear nozzle shape.

678

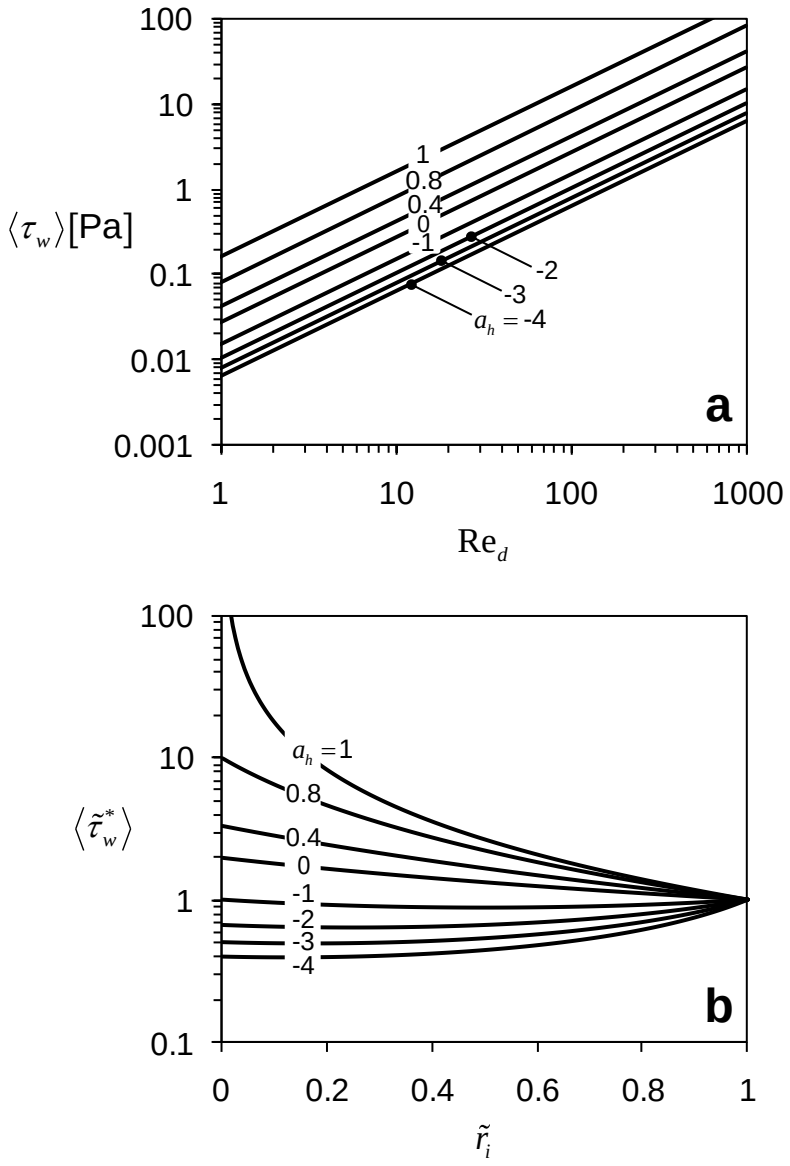

679

680

681 **Figure 5.** (*a*) Effect of Re_d on area-averaged shear stress $\langle \tau_w \rangle$ and (*b*) dimensionless area-
682 averaged shear stress $\langle \tilde{\tau}_w^* \rangle$ as a function of $\tilde{r}_i$', for different values of a_h for the case of
683 linear nozzle shape.

684

685

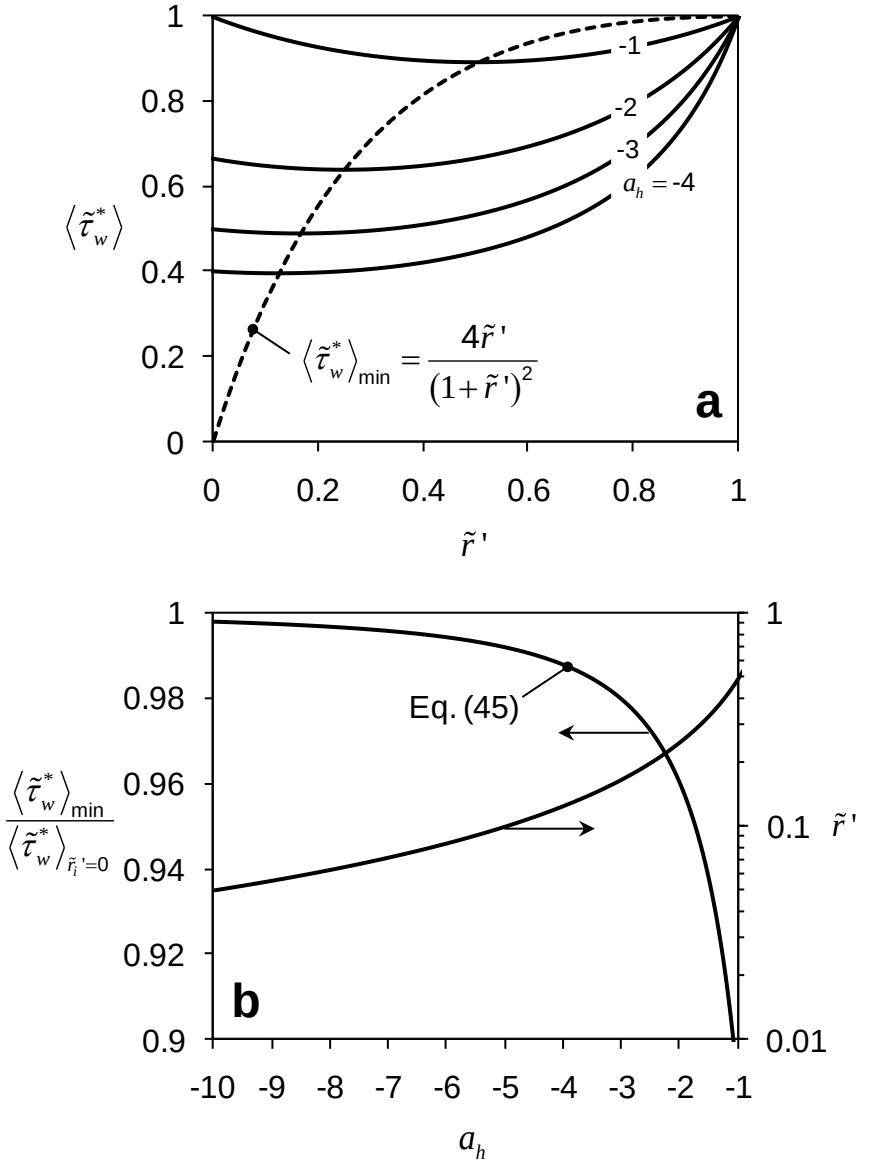

686

687

688 **Figure 6.** (*a*) Dimensionless area-averaged shear stress $\langle \tilde{\tau}_w^* \rangle$ as a function of $\tilde{r}_i'$ for selected
689 negative values of a_h showing the existence of a minimum $\langle \tilde{\tau}_w^* \rangle_{\min}$: loci of minima denoted
690 by the dashed line. (*b*) Evaluation of Eq. (45) showing the effect of a_h on loci position and
691 magnitude.

692

693

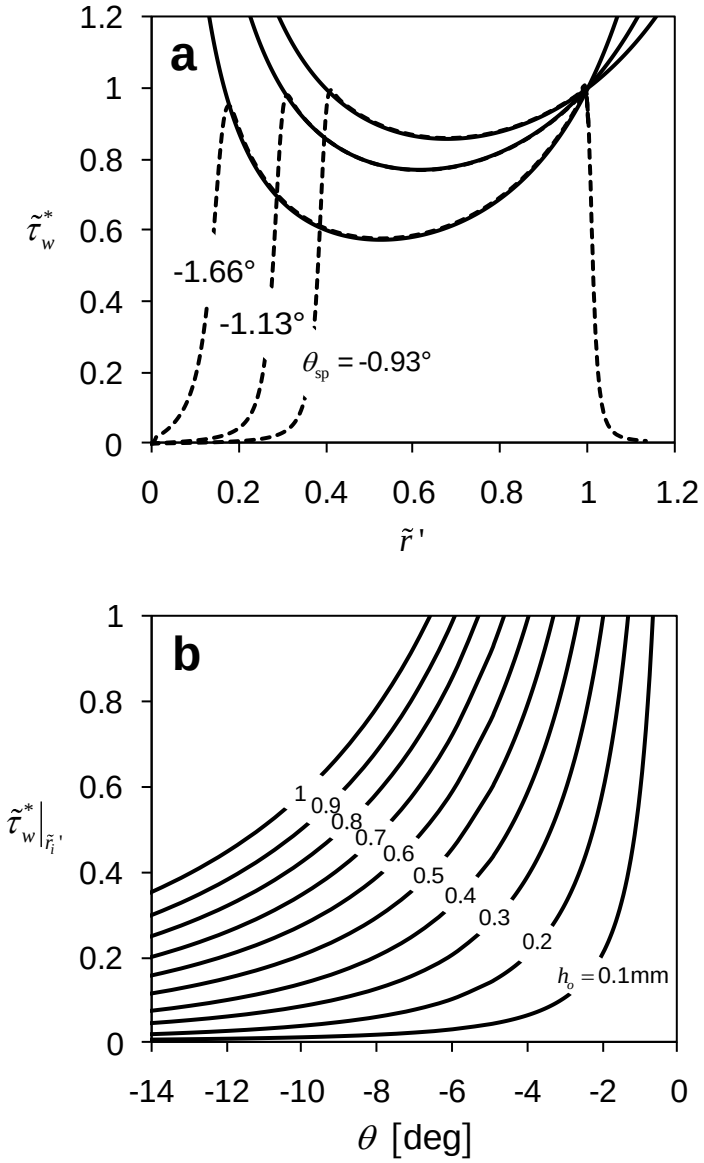

694

695

696 **Figure 7.** (*a*) Comparison of theoretical (Eq. (47), solid loci) and CFD simulated (dashed
697 loci) dimensionless shear stress $\tilde{\tau}_w^*$ profiles for selected values of θ_{sp}. (*b*) Dimensionless
698 shear stress evaluated at the inner radius of the nozzle ($\tilde{r}_i'$) as a function of the angle of the
699 nozzle rim for different values of h_o.

700

701

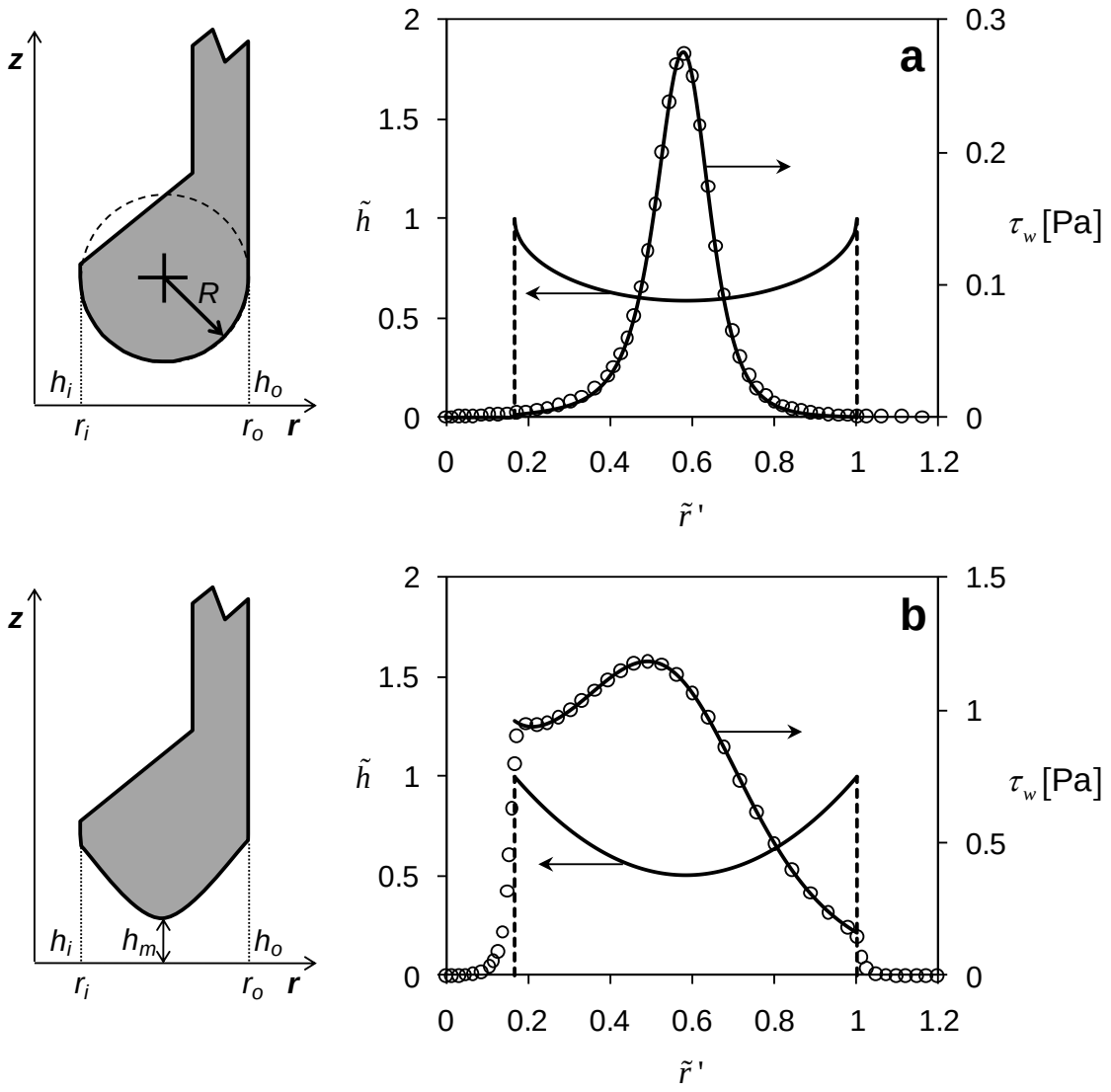

702

703

704 **Figure 8.** Comparison between shear stress profiles obtained analytically (solid loci) and
705 from CFD simulations (dashed loci) for (*a*) toroidal nozzle, (Eq. (50)) and (*b*) parabolic-
706 toroidal profile of $\tilde{h}$ ((Eq. (51)). CFD conditions: $\mathrm{Re}_d = 10$, h_o = 0.25 mm, r_i = 2.5 mm and
707 r_o = 15 mm.

708

709

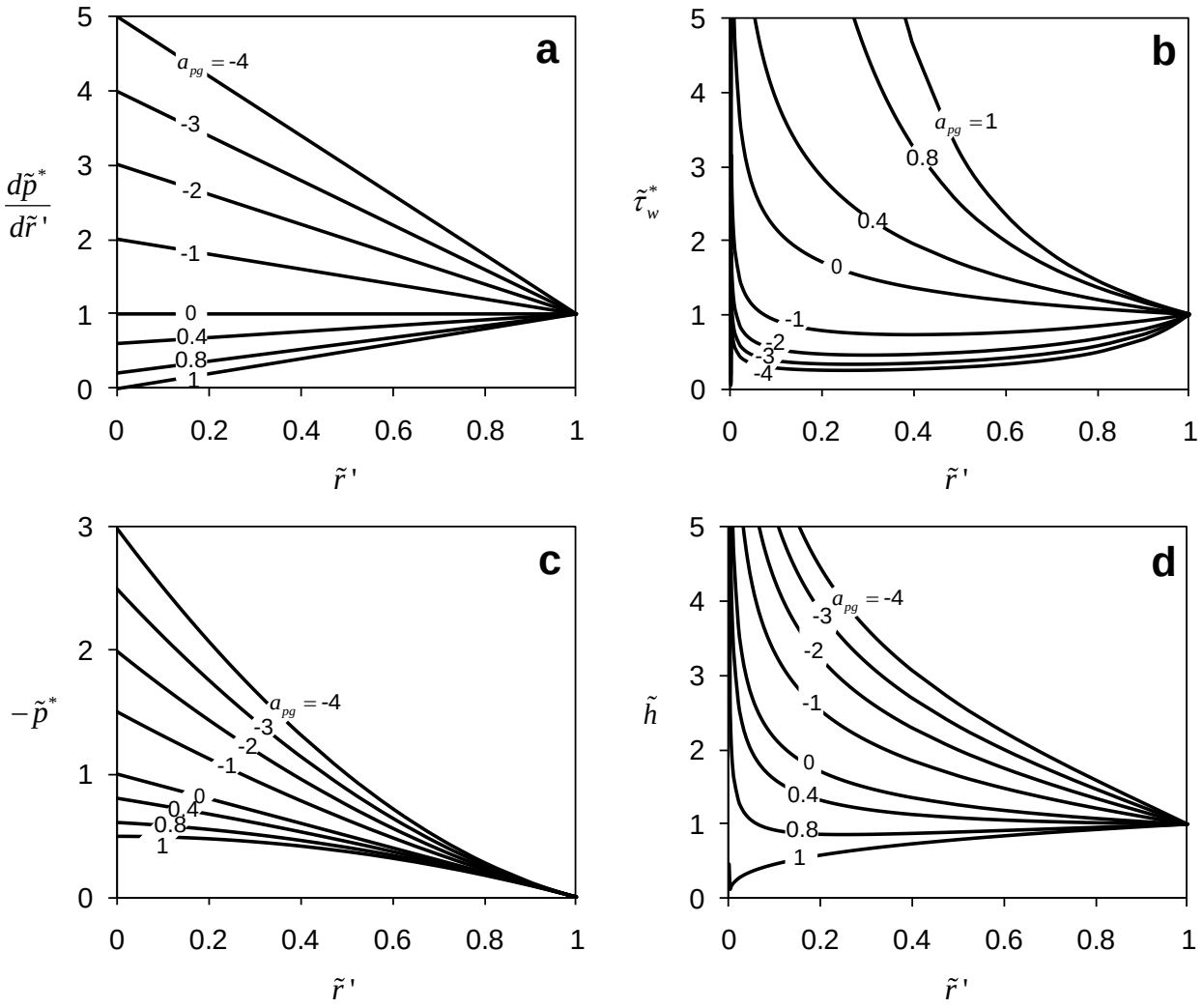

710

711

712 **Figure 9.** Dimensionless profiles of (*a*): pressure gradient ($d\tilde{p}^*/d\tilde{r}'$), (*b*) shear stress ($\tilde{\tau}_w^*$),

713 (*c*) pressure ($-\tilde{p}^*$), and (*d*): nozzle external geometry ($\tilde{h}$) as a function of the dimensionless

714 radial position ($\tilde{r}'$) for different values of a_{pg}, for the case of linear pressure gradient

715 profile.

716

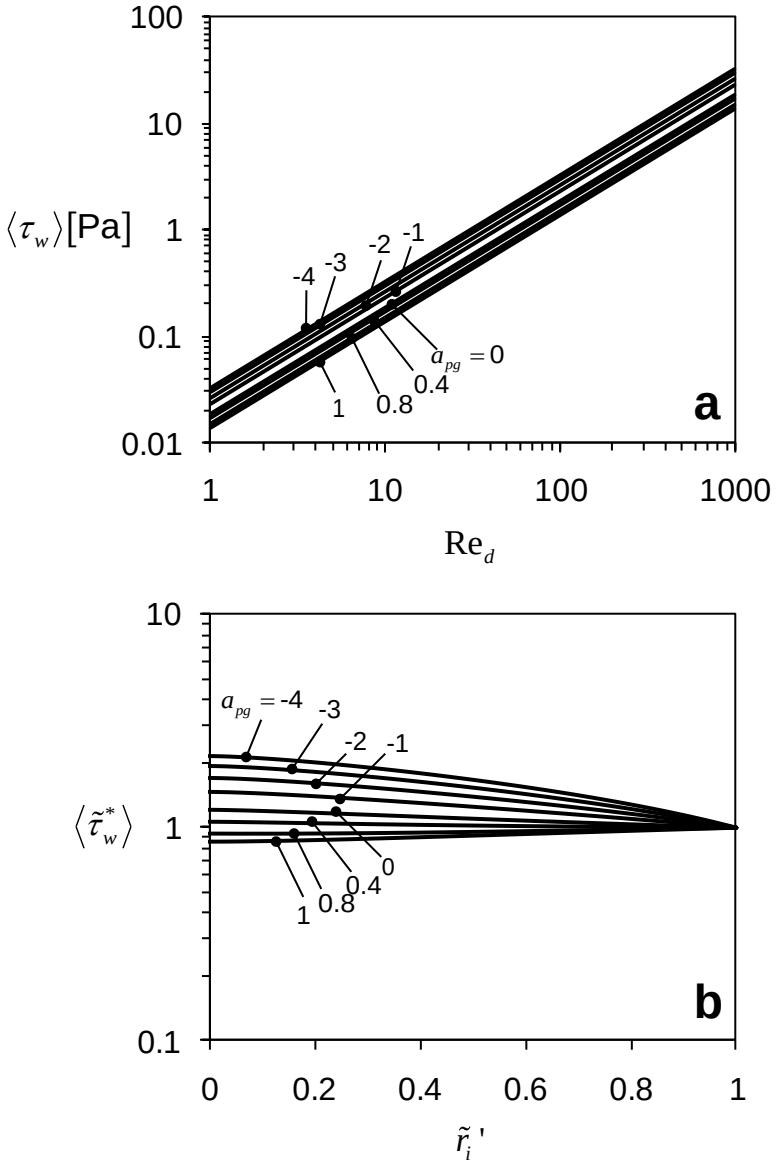

Figure 10. (*a*) Effect of Re_d on area-averaged shear stress $\langle \tau_w \rangle$ and (*b*) dimensionless area-averaged shear stress $\langle \tilde{\tau}_w^* \rangle$ as a function of $\tilde{r}_i$ ', for different values of a_{pg} for the linear pressure gradient profile case.

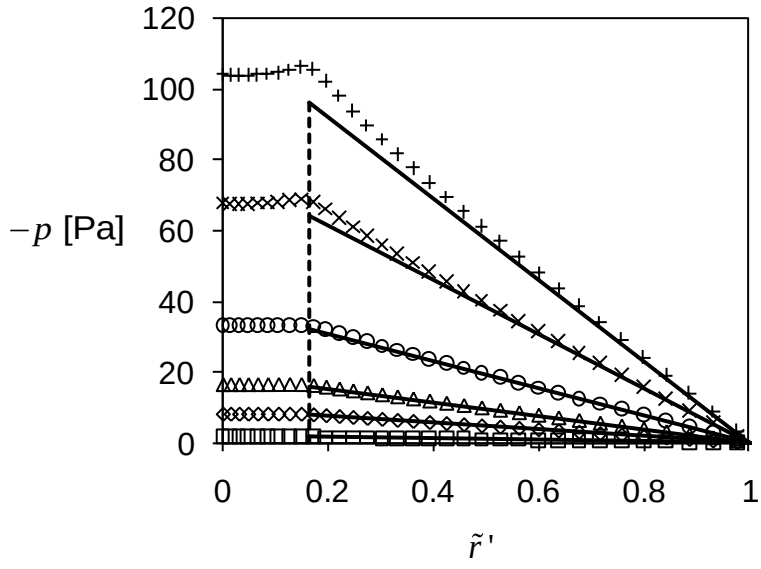

723

724

725 **Figure 11.** Comparison between theoretical (Eq. 57, solid loci) and CFD simulation
726 (symbols) of pressure as a function of $\tilde{r}'$ for different Re_d for the case of a linear pressure
727 profile. Symbols: (◊) Re_d = 1, (○) Re_d = 5, (△) Re_d = 10, (□) Re_d = 20, (×) Re_d = 40, and
728 (+) Re_d = 60. For each simulation: h_o = 0.25 mm, r_i = 2.5 mm and r_o = 15 mm.

729

730

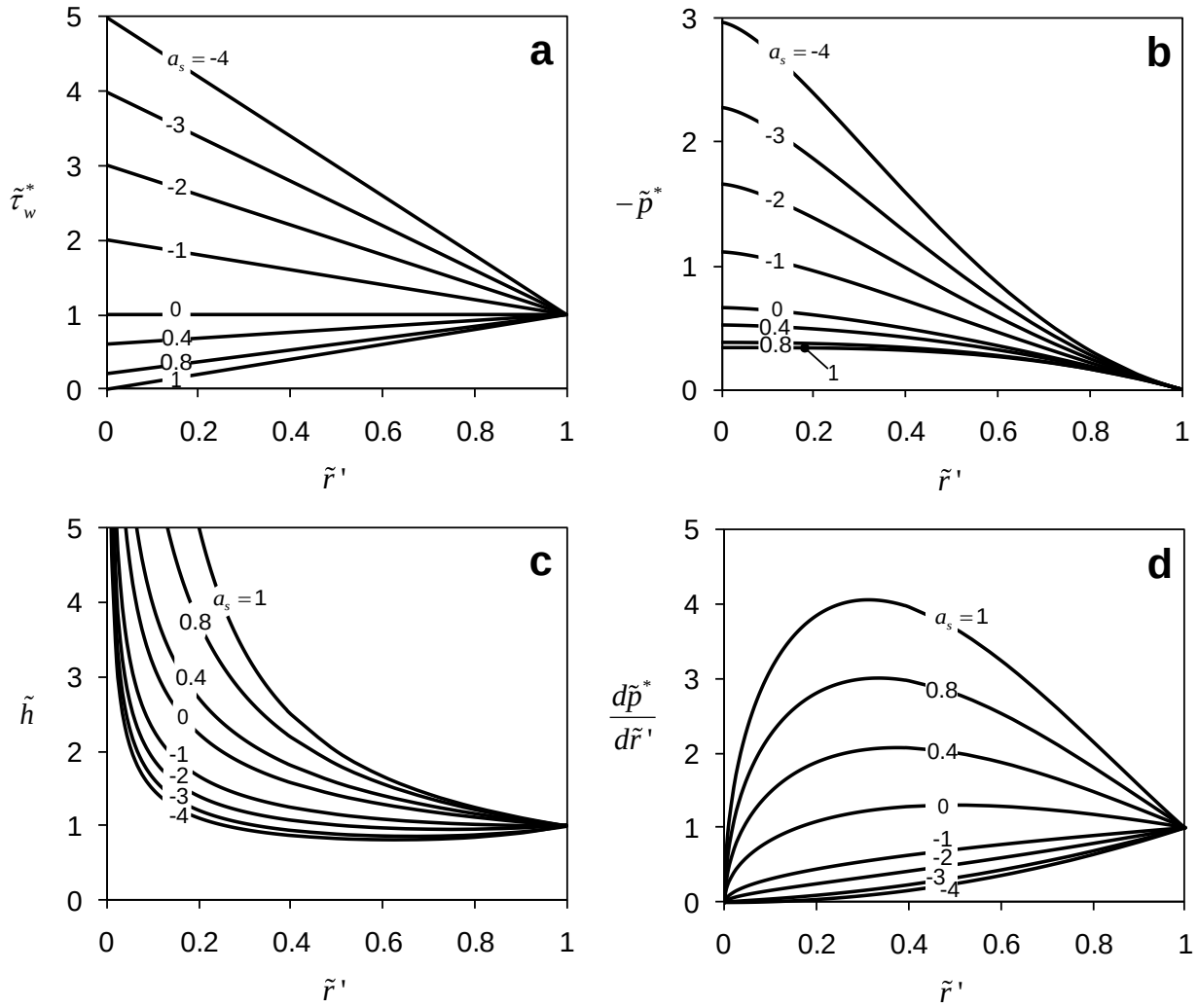

731

732

733 **Figure 12.** Dimensionless profiles of (*a*) shear stress ($\tilde{\tau}_w^*$), (*b*) pressure ($-\tilde{p}^*$), (*c*): nozzle
734 external geometry ($\tilde{h}$), and (*d*): pressure gradient ($d\tilde{p}^*/d\tilde{r}'$) as a function of the
735 dimensionless radial position ($\tilde{r}'$) for different values of a_s, for the case of linear shear
736 stress profile.

737

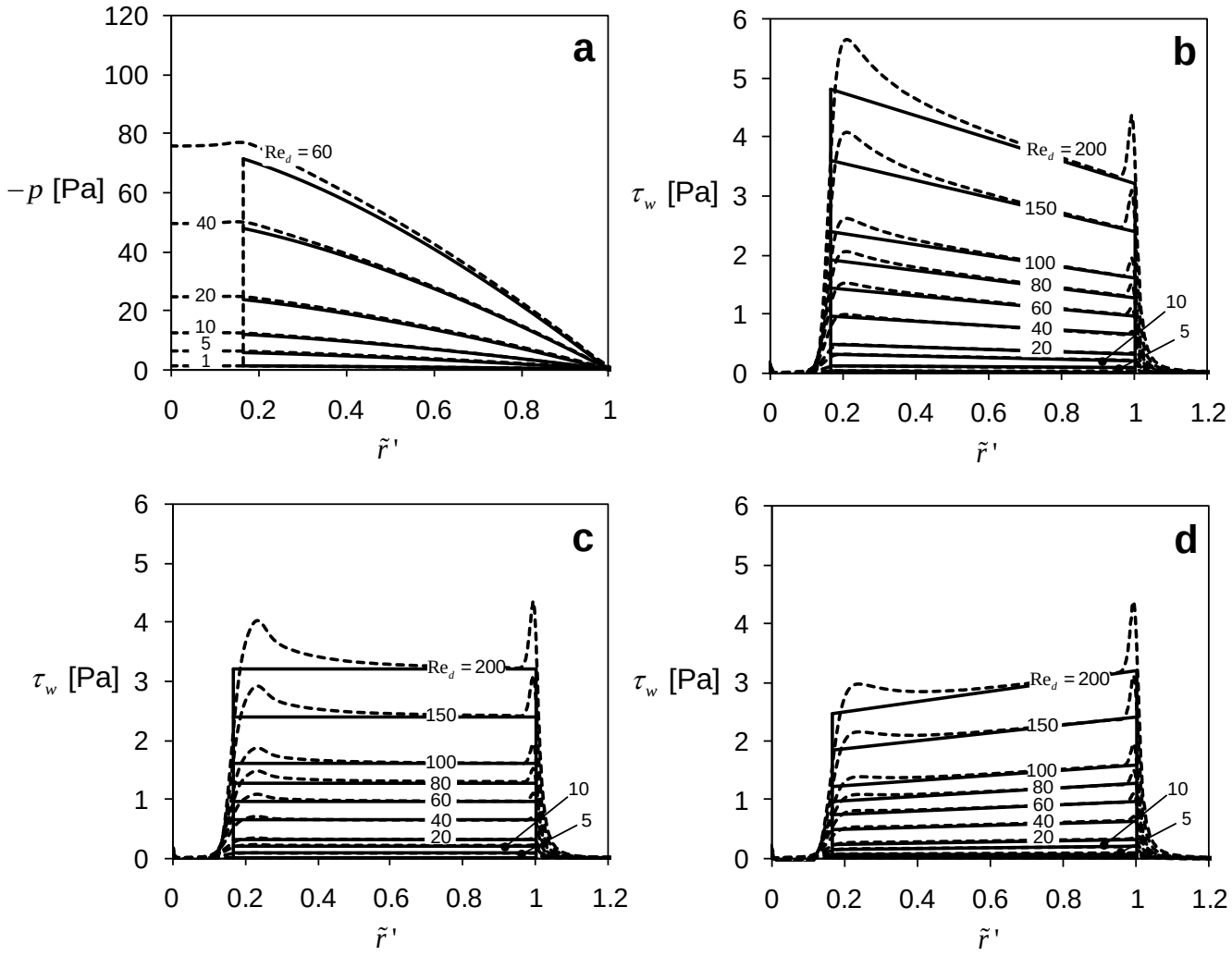

Figure 13. Comparison between CFD simulation (dashed loci) and analytical predictions (solid loci) of (*a*) pressure with $a_h = 0$ (Eq. 62) and shear stress values (Eq. (58)), for (*b*) $a_h = -0.7$, (*c*) and (*d*) $a_h = 0.25$, as a function of $\tilde{r}'$ for different Re_d. Conditions: h_o = 0.25 mm, r_i = 2.5 mm and r_o = 15 mm.

746

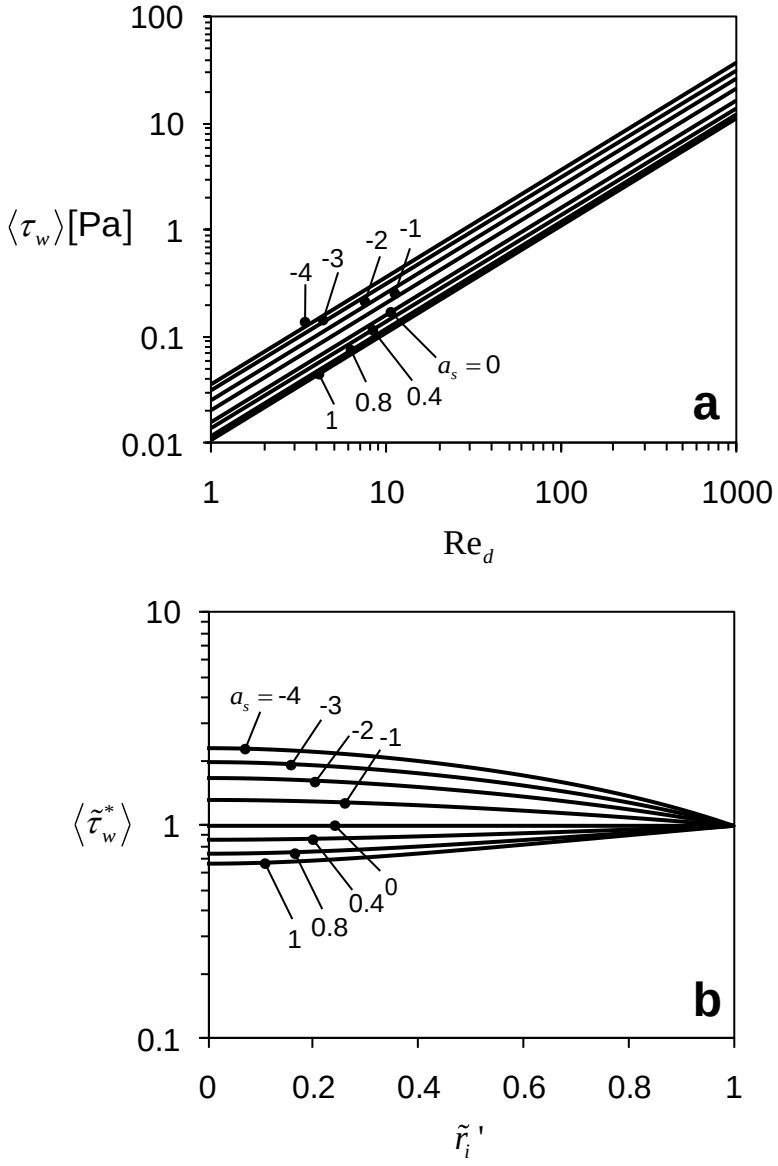

747

748

749 **Figure 14.** (*a*) Effect of Re_d on area-averaged shear stress $\langle \tau_w \rangle$ and (*b*) dimensionless area-
750 averaged shear stress $\langle \tilde{\tau}_w^* \rangle$ as a function of $\tilde{r}_i$ ', for different values of a_s for the linear shear
751 stress profile case.

752

753

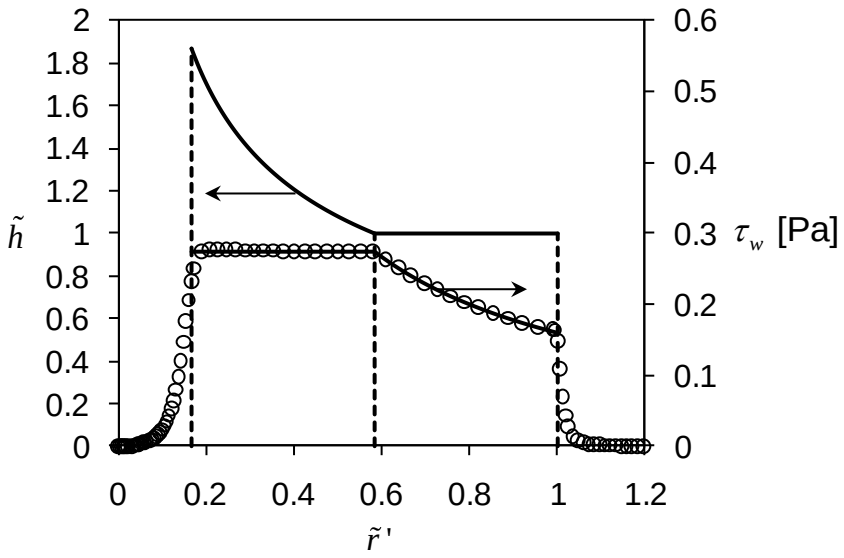

754

755

756 **Figure 15.** Shear stress values as a function of $\tilde{r}'$ for the example of a composite nozzle
757 with constant $\tilde{h}$ at the outer part of the nozzle and constant $\tilde{\tau}_w^*$ at the inner part (Re_d = 10,
758 h_o = 0.25 mm). Loci show the analytical model predictions and circles the values obtained
759 from CFD simulation.

760

761 **Table 1.** Expressions for $\tilde{h}$, $d\tilde{p}^*/d\tilde{r}'$ and $\tilde{\tau}_w^*$ using a general expression of the type $\tilde{f}(\tilde{r}')$

762 (within each row of the table) for either $\tilde{h}$, $d\tilde{p}^*/d\tilde{r}'$ or $\tilde{\tau}_w^*$.

763

$\tilde{h}$	$\frac{d\tilde{p}^*}{d\tilde{r}'}$	$\tilde{\tau}_w^*$
$\tilde{f}_h(\tilde{r}')$	$\frac{1}{\tilde{r}'\left[\tilde{f}_h(\tilde{r}')\right]^3}$	$\frac{1}{\tilde{r}'\left[\tilde{f}_h(\tilde{r}')\right]^2}$
$\frac{1}{\sqrt[3]{\tilde{r}'\,\tilde{f}_{pg}(\tilde{r}')}}$	$\tilde{f}_{pg}(\tilde{r}')$	$\sqrt[3]{\frac{\left[\tilde{f}_{pg}(\tilde{r}')\right]^2}{\tilde{r}'}}$
$\frac{1}{\sqrt{\tilde{r}'\,\tilde{f}_s(\tilde{r}')}}$	$\sqrt{\tilde{r}'\left[\tilde{f}_s(\tilde{r}')\right]^3}$	$\tilde{f}_s(\tilde{r}')$

764